Petroleum Science 21 (2024) 221–243

Contents lists available at ScienceDirect

Petroleum Science

journal homepage: www.keaipublishing.com/en/journals/petroleum-science

Original Paper

Analytical solution for the effective elastic properties of rocks with the tilted penny-shaped cracks in the transversely isotropic background

Zheng-Qian Ma [a, b], Xing-Yao Yin [a, b, c, *], Zhao-Yun Zong [a, b], Yuan-Yuan Tan [b], Ya-Ming Yang [b]

[a] National Key Laboratory of Deep Oil and Gas, China University of Petroleum (East China), Qingdao, 266580, Shandong, China
[b] School of Geosciences, China University of Petroleum (East China), Qingdao 266580, Shandong, China
[c] Pilot National Laboratory for Marine Science and Technology (Qingdao), Qingdao, 266200, Shandong, China

ARTICLE INFO

Article history:
Received 30 September 2022
Received in revised form
15 July 2023
Accepted 21 September 2023
Available online 13 October 2023

Edited by Jie Hao and Meng-Jiao Zhou

Keywords:
Effective elastic property
Tilted crack
Transverse isotropy
Analytical solution
Crack opening displacement

ABSTRACT

Seismic prediction of cracks is of great significance in many disciplines, for which the rock physics model is indispensable. However, up to now, multitudinous analytical models focus primarily on the cracked rock with the isotropic background, while the explicit model for the cracked rock with the anisotropic background is rarely investigated in spite of such case being often encountered in the earth. Hence, we first studied dependences of the crack opening displacement tensors on the crack dip angle in the coordinate systems formed by symmetry planes of the crack and the background anisotropy, respectively, by forty groups of numerical experiments. Based on the conclusion from the experiments, the analytical solution was derived for the effective elastic properties of the rock with the inclined penny-shaped cracks in the transversely isotropic background. Further, we comprehensively analyzed, according to the developed model, effects of the crack dip angle, background anisotropy, filling fluid and crack density on the effective elastic properties of the cracked rock. The analysis results indicate that the dip angle and background anisotropy can significantly either enhance or weaken the anisotropy degrees of the P- and SH-wave velocities, whereas they have relatively small effects on the SV-wave velocity anisotropy. Moreover, the filling fluid can increase the stiffness coefficients related to the compressional modulus by reducing crack compliance parameters, while its effects on shear coefficients depend on the crack dip angle. The increasing crack density reduces velocities of the dry rock, and decreasing rates of the velocities are affected by the crack dip angle. By comparing with exact numerical results and experimental data, it was demonstrated that the proposed model can achieve high-precision estimations of stiffness coefficients. Moreover, the assumption of the weakly anisotropic background results in the consistency between the proposed model and Hudson's published theory for the orthorhombic rock.

1. Introduction

Cracks widely distributed in all kinds of subsurface rocks have significant influences on the poroelastic, hydraulic and mechanical properties of reservoir media. Therefore, it is a research focus to characterize and predict the cracks in many fields, such as hydraulic fracturing (Lu et al., 2020), CO_2 sequestration (Kalra et al., 2018), exploration and exploitation of oil and gas reservoirs (Chen et al., 2018; Cheng et al., 2022). Rock physics models relating elastic coefficients to crack parameters are indispensable for accurately evaluating the crack distribution of the subsurface. Numerous rock physics models have been presented to calculate the effective elastic parameters of the cracked rock, including the Kuster and Toksoz model (Kuster and Toksöz, 1974), the differential effective medium model (Norris, 1985) and the self-consistent approximations model (O'Connell and Budiansky, 1974), and so forth. These early theoretical models are applicable to the case of randomly oriented cracks, whereas the subsurface cracks are frequently aligned owing to geological tectonism and stress orientation (Xu et al., 2018; Zhang et al., 2017; Zhao et al., 2020).

For the aligned cracks case, many researches have been

* Corresponding author. National Key Laboratory of Deep Oil and Gas, China University of Petroleum (East China), Qingdao, 266580, Shandong, China.
E-mail address: xyyin@upc.edu.cn (X.-Y. Yin).

https://doi.org/10.1016/j.petsci.2023.09.019

implemented. Hudson (1980) derived an expression of the effective stiffness matrix for the rock with isolated penny-shaped cracks in the isotropic background with the hypothesis of weak scattering. The expression is in the form of the sum of the background stiffness matrix and the first- and second-order stiffness contribution matrixes induced by the cracks. On this basis, Hudson (1988) and Hudson et al. (1996) investigated effects of partially saturated cracks and hydraulically connected cracks with fluid saturation on the effective elastic properties of the rock, respectively. Cheng (1993) also developed a model for calculating the effective stiffness coefficients of the rock with a set of spheroidal cracks based on Eshelby's static solution of the strain inside the inclusion. Although Cheng's model still requires low crack density due to no consideration of the interaction between cracks, it broadens the applicable range of the crack aspect ratio. Different from these two types of models, Schoenberg and Douma (1988) gave definitions of fracture compliance contribution matrixes (Schoenberg called them the fracture compliance matrixes) for fracture systems with different types of elastic behaviors (including monoclinic and orthorhombic behaviors, among many others). And the effective elastic matrix can be obtained by inverting the sum of the isotropic background compliance matrix and the fracture compliance matrix, which is called the linear-slip model (Schoenberg and Douma, 1988). Meanwhile, Schoenberg and Douma (1988) provided relationships between the fracture compliance elements and the fracture density only by comparing the linear-slip model with Hudson's model for the isolated crack case. Therefore, the accuracy and scope of application of the linear-slip model are the same as those of Hudson's model for the isolated crack case. In order to expand the scope of application of the linear-slip model, many researchers (Kachanov, 1992; Sevostianov and Kachanov, 1999) also derived the fracture compliance elements as functions of the fracture density based on the crack opening displacement (COD) tensor or the Eshelby tensor (Eshelby, 1957). Furthermore, by combining the linear-slip model and the anisotropic fluid substitution equation (Brown and Korringa, 1975), Huang et al. (2015) and Guo et al. (2017) analyzed effects of the fluid saturation on effective elastic properties of the fractured rock.

All the above theoretical models assume the background medium is isotropic. Nevertheless, naturally formed strata and even synthetic rock samples have non-negligible layered characteristics (Ding et al., 2017; Zhao et al., 2016a), which induces the VTI (vertically transverse isotropy) background. Hence, it is crucial to develop a rock physics model considering the effect of the VTI background on effective elastic properties of the cracked rock. To this end, Hoenig (1978) derived an integral form of the COD tensor for an elliptical crack in a generally anisotropic background. He further proved that the integral form can be simplified as a closed form only for rocks with the VTI background permeated by the elliptical crack parallel to the isotropic plane. Based on the explicit COD tensor, changes in moduli can be calculated. Jakobsen et al. (2003) and Zhao et al. (2016b) also deduced an integral expression for the effective stiffness tensor of the cracked rock with the arbitrarily anisotropic background using the T-matrix approach to study influences of elastic interactions between cracks on effective elastic properties. Withers (1989) investigated the explicit expression of the Eshelby tensor for the spheroidal crack in the isotropic plane of the VTI background and further calculated the effective elastic matrix of the cracked rock. Schoenberg and Helbig (1997) gave the expression of the effective stiffness matrix for the rock with the VTI background containing parallel vertical cracks, whereas relationships between the effective stiffness elements and the crack parameters are unknown. In addition, other studies have also been implemented for effective elastic properties of the cracked rock with the VTI background using other methods (Sevostianov et al., 2005; Xu et al., 2020). However, all these models are explicit only for the case with spheroidal cracks parallel to the isotropic plane of the VTI background, while for other more general cases, they are complicated integral forms. Numerical calculations of the integrals are required, which complicates applications of these models to geophysical predictions of fractured formations.

To investigate the analytical solution linking effective elastic properties of the rock with inclined cracks in the VTI background to microstructural parameters (e.g., crack density and dip angle), Hudson (1991) modeled the VTI background with an isotropic medium containing horizontal penny-shaped cracks. The effective elastic matrix of the rock with aligned cracks in the VTI background can be estimated by taking the sum of the stiffness matrix of the isotropic medium and two groups of stiffness correction matrixes induced by the real cracks and the hypothetic cracks. However, this result is inapplicable to the case with relatively high degrees of the background anisotropy owing to underestimating elastic interactions between the real cracks and the VTI background. And the accuracy of the model depends on choice of the isotropic matrix parameters. Besides, Guerrero et al. (2007) found through two simple numerical experiments that the COD tensor of the circular crack embedded in the elliptic VTI background might be weakly dependent on the dip angle of the crack. Based on this conclusion, Guo et al. (2019, 2021) deduced approximate expressions for the effective elastic matrixes of rocks with the VTI backgrounds permeated by tilted penny-shaped and elliptical cracks, respectively. However, predicted results of the approximate solution have relatively high errors in some cases (refer to the first subsection of "Discussion") and even are not entirely accurate for the isotropic background (a type of elliptic anisotropy) case. Hence, more work needs to be done to obtain a more reasonable and accurate explicit solution for the effective stiffness matrix of the rock with the tilted cracks in the VTI background.

In this work, we first study dependences of CODs on the crack dip angle by forty groups of numerical experiments. Based on the result of the experiments, we derive the explicit expression of the compliance matrix of the rock with the tilted cracks in the VTI background. According to the developed model, we further investigate effects of the crack dip angle, background anisotropy, fluid and crack density on the effective elastic properties of the rock. Finally, the proposed model is proven reasonable and of high precision by comparing with accurate numerical results and experimental data. Moreover, it is consistent with the published theory under the hypothesis of the weakly anisotropic background.

2. Theory

2.1. Theoretical background

As shown in Fig. 1, we consider a reference volume V containing an ellipsoidal inclusion of a volume V^*. The effective compliance tensor $\mathbf{S}^{\mathrm{eff}}$ of the reference volume can be written as

$$s_{ijkl}^{\mathrm{eff}} = s_{ijkl}^{0} + h_{ijkl}, \tag{1}$$

where s_{ijkl}^{0} and h_{ijkl} denote the compliance tensor of the background medium and the compliance contribution tensor of the inclusion, respectively. The compliance tensor is the reciprocal of the stiffness

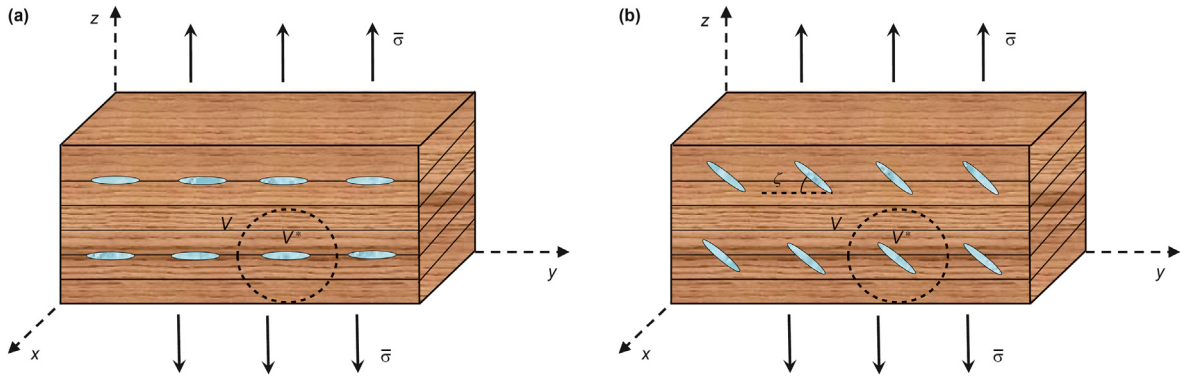

Fig. 1. Schematics of media with the VTI background containing aligned ellipsoidal inclusions. The inclusions are (a) parallel to and (b) inclined to the isotropic plane of the VTI background, respectively. The plane *xoy* is parallel to the isotropic plane.

tensor. The compliance contribution tensor $\mathbf{H}$ (h_{ijkl}) can be represented as follows (Sevostianov et al., 2005)

$$h_{ijkl} = c^* \left[\left(s^*_{ijkl} - s^0_{ijkl} \right)^{-1} + c^0_{ijpq} \left(I_{pqkl} - P_{pqrs} c^0_{rskl} \right) \right]^{-1}, \tag{2}$$

where the weight $c^* = V^*/V$ is the volume fraction of the inclusion and s^*_{ijpq} is the compliance tensor of the inclusion. The symbols c^0_{ijrs} and I_{ijkl} denote the stiffness tensor of the background medium and the unit fourth-order tensor, respectively. And P_{rspq} is the Hill tensor, which can be calculated by the integral of the Green function $G_{ij}(x - x')$ of the background medium, that is,

$$P_{ijkl} = -\frac{1}{4} \int_V \left(\frac{G_{ik}}{x_j x_l} + \frac{G_{jk}}{x_i x_l} + \frac{G_{il}}{x_j x_k} + \frac{G_{jl}}{x_i x_k} \right) \mathrm{d}V(x')$$

(Giraud et al., 2007). The repeated indices refer to the Einstein's summation convention. Assuming that the number of the same aligned inclusions is υ in the reference volume V, their ith semi-axis length is a_i and there are no elastic interactions between the inclusions, the total compliance contribution tensor $\mathbf{H}$ of the empty inclusions can be deduced as

$$h_{ijkl} = \varphi_c \left[c^0_{ijpq} \left(I_{pqkl} - P_{pqrs} c^0_{rskl} \right) \right]^{-1}. \tag{3}$$

In Eq. (3), $\varphi_c = \frac{4\pi a_1 a_2 a_3 \upsilon}{3V}$ denotes the porosity of the cavities. For the penny-shaped crack modeled by an extremely oblate spheroidal inclusion, $a_1 = a_2 = a$, and $\alpha = a_3/a \to 0$ defined as the aspect ratio of the crack. Its porosity is $\varphi_c = \frac{4\pi\alpha}{3} e$, where $e = a^3\upsilon/V$ is called the crack density. Since we neglect the elastic interactions between the inclusions, Eq. (3) is applicable to the case of the rock containing dilute concentration of cracks that is common underground (Chen and Zhang, 2017; Liu et al., 2018). For simplicity, we will next focus on the rock with dilute concentration of cracks. Note that the interactions between the cracks and the anisotropic background will be involved.

For any flat crack (with α tending to zero), the compliance contribution tensor can also be obtained by (Seyedkavoosi et al., 2018)

$$h_{ijkl} = \frac{S}{4V} \left(n_i B_{jk} n_l + n_j B_{ik} n_l + n_i B_{jl} n_k + n_j B_{il} n_k \right), \tag{4}$$

where n_i represents the ith component of the normal vector of the flat crack surface. The symbol S means the area of the crack surface. The second-rank tensor $\mathbf{B}$ (B_{ij}) is called the crack opening displacement (COD) tensor, combining the average crack displacement discontinuity vector $\vec{\mathbf{b}}$ with the uniform traction $\vec{\mathbf{t}} = \bar{\boldsymbol{\sigma}} \bullet \vec{\mathbf{n}}$ induced by the remotely applied uniform stress field $\bar{\boldsymbol{\sigma}}$ at the crack site in the absence of the crack, namely $\vec{\mathbf{b}} = \mathbf{B} \bullet \vec{\mathbf{t}}$. Accordingly, the COD tensor $\mathbf{B}$ of the penny-shaped crack embedded in the VTI background as in Fig. 1b can also be calculated from the known $\mathbf{H}$. Specifically, the explicit expressions of the derivatives of the Green function for the VTI matrix are utilized to numerically estimate the Hill tensor $\mathbf{P}$ (P_{ijkl}) with the Gauss-Legendre quadrature (Giraud et al., 2007). Then, the compliance contribution tensor $\mathbf{H}$ calculated based on Eq. (3) is used to settle Eq. (4) for obtaining the COD tensor $\mathbf{B}$.

For the dry penny-shaped crack in the isotropic plane of the VTI background, as shown in Fig. 1a, Fabrikant (1989) gave an analytical form of the COD tensor $\mathbf{B}^{\mathrm{hor}}$. We rewrite the analytical form in terms of Thomsen's anisotropic parameters as

$$B^{\mathrm{hor}}_{11} = B^{\mathrm{hor}}_{22} = \frac{16aG}{3\pi c^0_{33} \left[g\sqrt{1+2\gamma}\, G + c^0_{33} \left(1 + 2\varepsilon - \xi^2 \right) \sqrt{g} \right]}, \tag{5}$$

$$B^{\mathrm{hor}}_{33} = \frac{8aG}{3\pi \left(c^0_{33} \right)^2 \left(1 + 2\varepsilon - \xi^2 \right) \sqrt{g/(1+2\varepsilon)}}, \tag{6}$$

$$G = c^0_{33} \sqrt{\left(\sqrt{1+2\varepsilon} - \xi \right) \left(\sqrt{1+2\varepsilon} + \xi + 2g \right)} \tag{7}$$

and other components are zero. In Eqs. (5) and (6), B^{hor}_{11} (or B^{hor}_{22}) and B^{hor}_{33} represent the tangential and normal CODs of the crack in the isotropic plane of the VTI background, respectively. The symbol c^0_{ij} denotes the stiffness matrix of the VTI background in the Voigt's concise form. The variables $g = c^0_{44}/c^0_{33}$ and $\xi = -g + (1 - g)[1 + 2\delta/(1-g)]^{1/2}$. Thomsen's anisotropic parameters $\varepsilon = \frac{c^0_{11} - c^0_{33}}{2c^0_{33}}$, $\gamma = \frac{c^0_{66} - c^0_{44}}{2c^0_{44}}$ and $\delta = \frac{(c^0_{13} + c^0_{44})^2 - (c^0_{33} - c^0_{44})^2}{2c^0_{33}(c^0_{33} - c^0_{44})}$ (Thomsen, 1986). By substituting Eqs. (5) and (6) into Eq. (4), we can obtain the analytical solution of the compliance contribution tensor $\mathbf{H}$. However, for the inclined penny-shaped crack, we cannot directly give the analytical forms of its exact compliance contribution tensor $\mathbf{H}$ and COD tensor $\mathbf{B}$, owing to difficulty in obtaining the exact analytical expression of its Hill tensor.

By making ε, γ and δ equal zero in Eqs. (5)–(7), we can derive the COD tensor of the dry crack in the isotropic background, which reflects the normal and tangential CODs in the crack plane without the effect of background anisotropy. The difference between the normal and tangential CODs can be deduced as

$$\left(B_{22}^{\mathrm{hor}}-B_{33}^{\mathrm{hor}}\right)\Big|_{\varepsilon,\gamma,\delta=0}=\frac{4a}{3\pi g c_{33}^{0}}\frac{1-2g}{(3-2g)(1-g)}\Bigg|_{\varepsilon,\gamma,\delta=0}. \tag{8}$$

For the isotropic medium, g means the square of the ratio of the S-wave velocity to the P-wave velocity and its value varies from 0 to 0.5 due to Poisson's ratio ranging from 0 to 0.5. This results in $(B_{22}^{\mathrm{hor}}-B_{33}^{\mathrm{hor}})\big|_{\varepsilon,\gamma,\delta=0}>0$, which implies the tangential COD of the dry penny-shaped crack in the isotropic background is larger than the normal COD for most cases. This characteristic is called the intrinsic property of the crack. Fig. 2 demonstrates effects of c_{33}^{0}, ε, γ, δ and g on B_{33}^{hor} and B_{22}^{hor} of the dry penny-shaped crack in the isotropic plane of the VTI background. From Fig. 2a, it can be found that the effects of c_{33}^{0} on B_{22}^{hor} and B_{33}^{hor} are almost identical, which are caused by the fact that both B_{22}^{hor} and B_{33}^{hor} are linear functions of $(c_{33}^{0})^{-1}$. Fig. 2b, 2c and 2e indicates that B_{22}^{hor} and B_{33}^{hor} decrease with ε, γ and g increasing and influences of ε, γ and g on B_{22}^{hor} are larger than those on B_{33}^{hor}. Fig. 2d reveals that the increasing rate of B_{33}^{hor} with δ is higher than that of B_{22}^{hor}. By integrating Fig. 2a–e, we can draw conclusions that with increases of the ε, γ and δ, the increasing effects of the background anisotropy on the CODs induce that $(B_{22}^{\mathrm{hor}}-B_{33}^{\mathrm{hor}})$ varies from greater than zero to less than zero. Therefore, when $(B_{22}^{\mathrm{hor}}-B_{33}^{\mathrm{hor}})>0$, it can be considered that the intrinsic property of the crack has the leading influences on the CODs. When $(B_{22}^{\mathrm{hor}}-B_{33}^{\mathrm{hor}})<0$, we can think that the effects of the background anisotropy on the CODs surpass those of the intrinsic property of the crack and become dominant influences.

2.2. Approximate explicit solution of COD tensor of a dry tilted penny-shaped crack in the VTI background

The compliance contribution tensor is the function of the COD tensor, as given in Eq. (4). We will study the explicit expression of

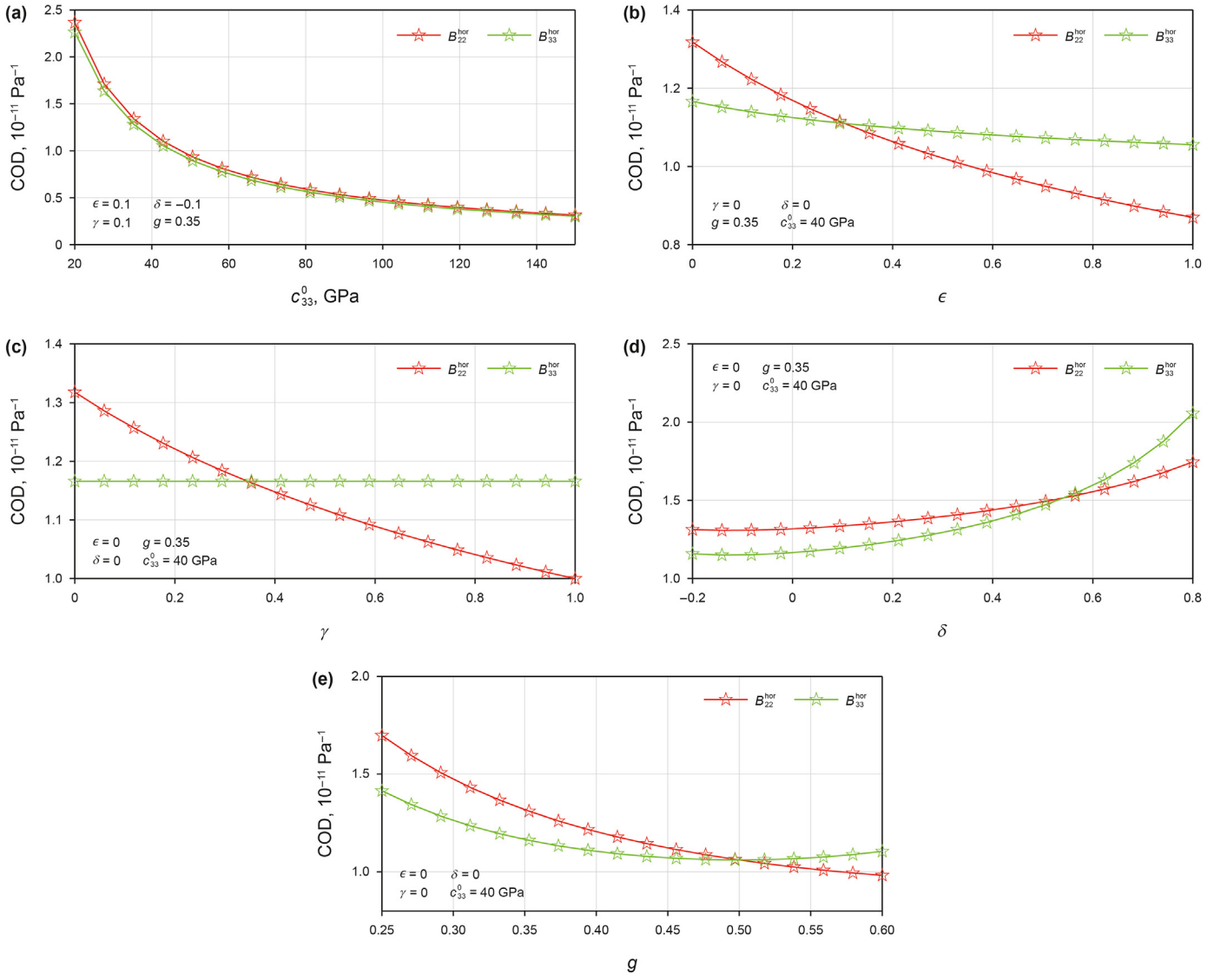

Fig. 2. Variations of B_{22}^{hor} and B_{33}^{hor} with (a) c_{33}^{0}, (b) ε, (c) γ, (d) δ and (e) g.

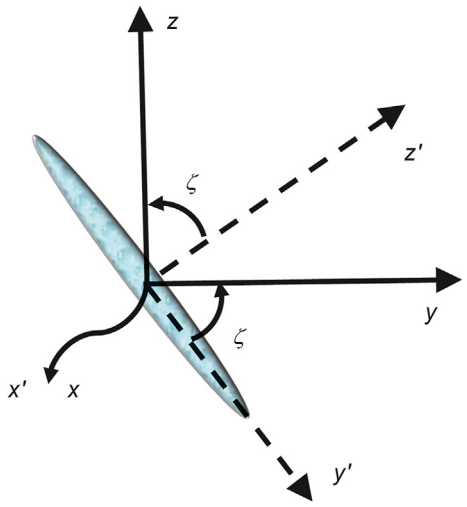

Fig. 3. Comparison between the *xyz* system (solid lines) and the *x′y′z′*system (dashed lines).

the COD tensor in order to derive the analytical form of the effective elastic matrix of the rock with inclined cracks in the VTI background. For such rock, we adopt two coordinate systems to characterize its properties, as shown in Fig. 3. One is the *xyz* system represented by three orthogonal solid lines, which has been applied in Fig. 1. The other is the *x′y′z′* system represented by three orthogonal dashed lines, in which the *x′* axis is accordant with the *x* axis and the *z′* axis is normal to the crack plane. Obviously, for the isotropic background case (in which the intrinsic property of the crack is the main influence factor of the CODs), the COD tensor in the *x′y′z′* system is independent of the crack dip angle. A second-order tensor $\mathbf{A}^{\mathrm{b}}$ in the *xyz* system can be transformed into a new representation $\mathbf{A}^{\mathrm{n}}$ in the *x′y′z′* system and the transformation form is

$$A_{ij}^{\mathrm{b}} = L_{im}A_{mn}^{\mathrm{n}}L_{jn} \tag{9}$$

and

$$\mathbf{L} = \begin{bmatrix} 1 & 0 & 0 \\ 0 & \cos\zeta & \sin\zeta \\ 0 & -\sin\zeta & \cos\zeta \end{bmatrix}. \tag{10}$$

In Eq. (10), ζ is the dip angle of the crack, which equals the angle between the *z* axis and *z′* axis as shown in Fig. 3.

Forty groups of VTI rocks are used as background media to analyze the dependence of the COD tensor of the dry penny-shaped crack on the crack dip angle. The first 35 groups of the VTI rocks are induced by aligned arrangement or crystal lattice of minerals, and their measured stiffness coefficients are shown in Table A−1 of Appendix A. The last 5 groups of the VTI rocks are induced by horizontal aligned fractures in an isotropic matrix consisting of 80 percent quartz and 20 percent clay by volume. The bulk moduli, shear moduli and mass densities of the quartz and clay are 76.8 GPa, 32 GPa, 2.71 g/cm^3, and 21 GPa, 7 GPa, 2.6 g/cm^3, respectively. The horizontal fractures with an aspect ratio of 0.01 are filled with the fluid with the bulk modulus of 1 GPa, and their densities are 0, 0.0125, 0.025, 0.0375 and 0.05 in sequence. The Voigt-Reuss-Hill average is utilized to calculate properties of the isotropic matrix and the Eshelby-Cheng model (Cheng, 1993) is adopted to estimate stiffness coefficients of the last 5 groups of the VTI rocks. The penny-shaped crack is simulated by the spheroidal inclusion with the aspect ratio of 0.01, and its dip angle ranges from 0° to 90°. The COD tensors of the designed models can be calculated by Eqs. (3) and (4). Moreover, the COD tensor in the *xyz* system can be transformed into the COD tensor in the *x′y′z′*system by using Eqs. (9) and (10), namely

$$\mathbf{B}^{\mathrm{n}} = \mathbf{L}^{\mathrm{T}}\mathbf{B}^{\mathrm{b}}\mathbf{L} \tag{11}$$

where

$$\mathbf{B}^{\mathrm{b}} = \begin{bmatrix} B_{11}^{\mathrm{b}} & B_{12}^{\mathrm{b}} & B_{13}^{\mathrm{b}} \\ B_{12}^{\mathrm{b}} & B_{22}^{\mathrm{b}} & B_{23}^{\mathrm{b}} \\ B_{13}^{\mathrm{b}} & B_{23}^{\mathrm{b}} & B_{33}^{\mathrm{b}} \end{bmatrix} \text{ and } \mathbf{B}^{\mathrm{n}} = \begin{bmatrix} B_{11}^{\mathrm{n}} & B_{12}^{\mathrm{n}} & B_{13}^{\mathrm{n}} \\ B_{12}^{\mathrm{n}} & B_{22}^{\mathrm{n}} & B_{23}^{\mathrm{n}} \\ B_{13}^{\mathrm{n}} & B_{23}^{\mathrm{n}} & B_{33}^{\mathrm{n}} \end{bmatrix}. \tag{12}$$

In Eq. (11), $\mathbf{B}^{\mathrm{b}}$ and $\mathbf{B}^{\mathrm{n}}$ represent the COD tensors expressed in the *xyz* and *x′y′z′* systems, respectively. We define changes of the CODs of the crack inclined by ζ degrees relative to the CODs of the horizontal crack as

$$\Delta_{ij}^{**}(\zeta) = \left|B_{ij}^{*}(\zeta) - B_{ij}^{*}(\zeta = 0^\circ)\right| \Big/ B_{ij}^{*}(\zeta = 0^\circ) \quad (i, j = 1, 2, 3). \tag{13}$$

In Eq. (13), the operator $|\bullet|$ means taking the absolute values. The symbol $B_{ii}^{*}(\zeta)$ represents the *ij* element of $\mathbf{B}^{\mathrm{b}}$ or $\mathbf{B}^{\mathrm{n}}$ of the crack with the ζ dip angle and Δ_{ij}^{**} is the relative change of the *ij* element. Fig. 4 demonstrates variations of the CODs and Δ_{ii}^{**} of the crack in the 10th VTI background with respect to the dip angle. Fig. 5 displays variations of ratios of the off-diagonal elements to the 3rd diagonal element of the COD tensor of the crack in the 10th VTI background with the dip angle. The descriptions of Figs. 6 and 7 are similar to those of Figs. 4 and 5, respectively, with the exception of the VTI background parameters from the 17th group. Fig. 8 exhibits relative differences between B_{22}^{hor} and B_{33}^{hor} of the dry cracks in the isotropic planes of forty groups of VTI backgrounds, and the relative differences are calculated by

$$\Delta_{\mathrm{COD}}^{\mathrm{H}} = 2\left(B_{22}^{\mathrm{hor}} - B_{33}^{\mathrm{hor}}\right) \Big/ \left(B_{22}^{\mathrm{hor}} + B_{33}^{\mathrm{hor}}\right). \tag{14}$$

The sign of $\Delta_{\mathrm{COD}}^{\mathrm{H}}$ is the same as that of $(B_{22}^{\mathrm{hor}} - B_{33}^{\mathrm{hor}})$. From Fig. 4, we can find that for the 10th VTI background case, the diagonal elements of the COD tensor are less dependent on the crack dip angle in the *x′y′z′* system than in the *xyz* system. The reason is that $\Delta_{\mathrm{COD}}^{\mathrm{H}} > 0$ for the 10th VTI background case, as seen in Fig. 8. The intrinsic property of the crack is the major influence factor of the CODs. Hence, the diagonal elements of the COD tensor vary more feebly with the dip angle in the *x′y′z′* system than in the *xyz* system. Comparing Fig. 5a with 5b, it can be seen that for the 10th VTI background case, the ratios of the off-diagonal components to the 3rd diagonal component of the COD tensor are far smaller in the *x′y′z′* system than in the *xyz* system. In consequence, the off-diagonal components of the COD tensor in the *x′y′z′* system are negligible for the case with $\Delta_{\mathrm{COD}}^{\mathrm{H}} > 0$. Analogously, Fig. 6 illustrates that the diagonal elements of the COD tensor are less dependent on the dip angle in the *xyz* system than in the *x′y′z′* system for the 17th VTI background case. The result is caused by the fact that $\Delta_{\mathrm{COD}}^{\mathrm{H}} < 0$ for the 17th VTI background case, as shown in Fig. 8. The background anisotropy is the dominant influence factor of the CODs. Fig. 7 reveals that the ratios of the off-diagonal elements to the 3rd diagonal component of the COD tensor in the *xyz* system are comparatively small and smaller than those in the *x′y′z′* system for the 17th VTI background case. Hence, the off-diagonal components of the COD tensor in the *xyz* system can be set to zero with

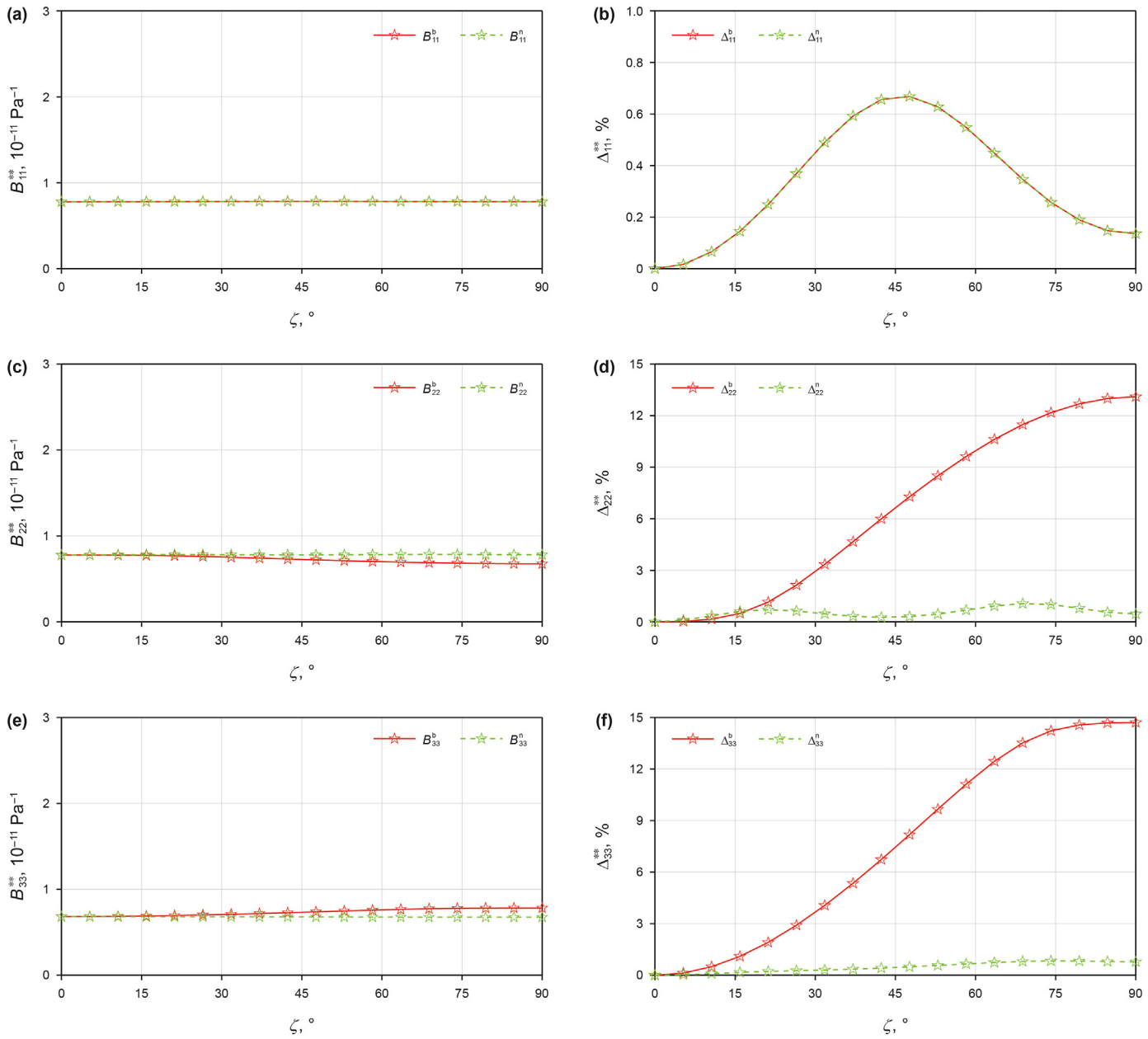

Fig. 4. Comparisons between dependences of diagonal elements of the COD tensors in the *xyz* system (red lines) and the *x′y′z′* system (green lines) on the dip angle of the crack in the 10th VTI background. Fig. (a), (c) and (e) shows the variations of B_{ii} ($i = 1, 2, 3$) with the dip angle, respectively. Fig. (b), (d) and (f) demonstrates variations of Δ_{ii}^{**} ($i = 1, 2, 3$) with the dip angle, respectively.

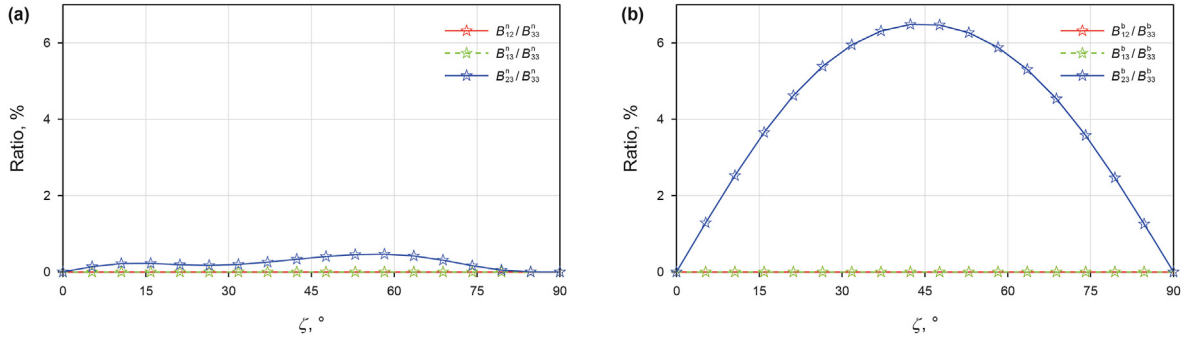

Fig. 5. Variations of ratios of the off-diagonal elements to the 3rd diagonal element of the COD tensor of the crack in the 10th VTI background with the dip angle. The COD tensors are in (a) the *x′y′z′* system and (b) the *xyz* system, respectively.

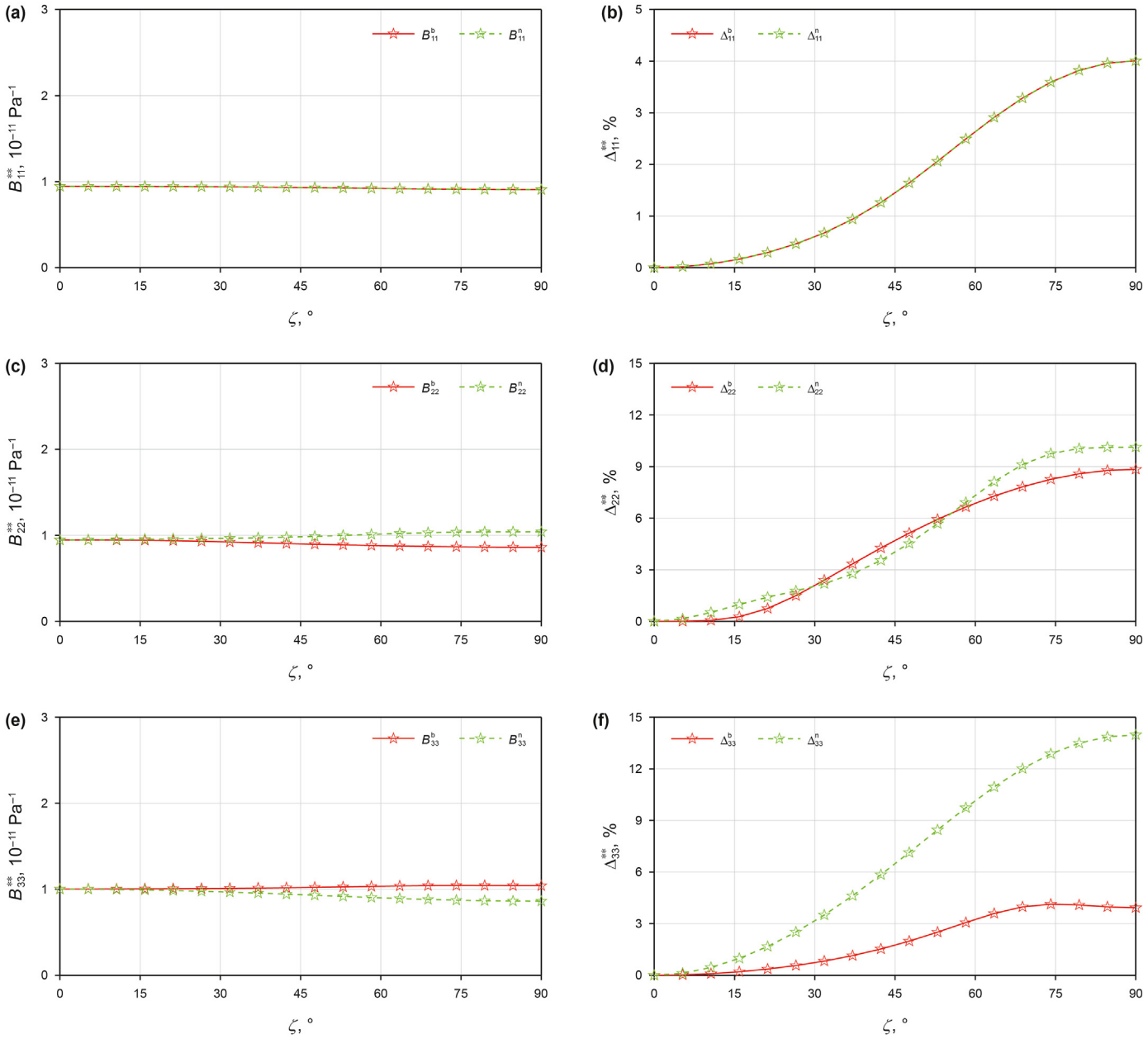

Fig. 6. Comparisons between dependences of diagonal elements of the COD tensors in the *xyz* system (red lines) and the *x′y′z′* system (green lines) on the dip angle of the crack in the 17th VTI background. The descriptions of Fig. (a)–(f) are similar to those of Fig. 4a–f.

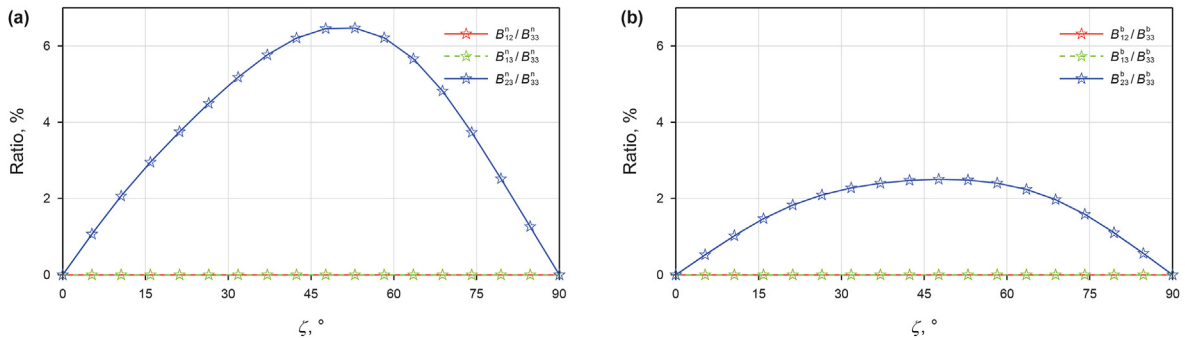

Fig. 7. Variations of ratios of the off-diagonal elements to the 3rd diagonal element of the COD tensor of the crack in the 17th VTI background with the dip angle. The COD tensors are in (a) the *x′y′z′* system and (b) the *xyz* system, respectively.

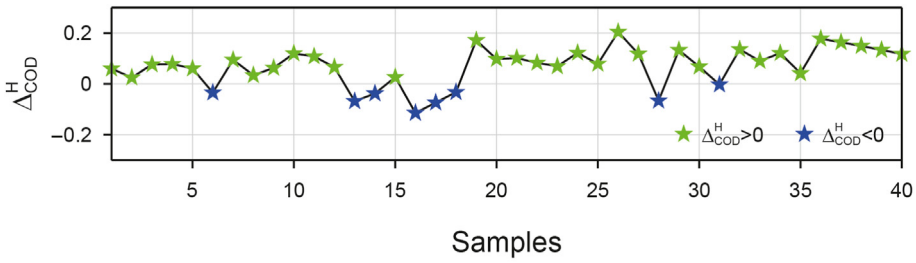

Fig. 8. Δ^{H}_{COD} of dry cracks in the isotropic planes of forty VTI backgrounds.

satisfactory accuracies for the case with Δ^{H}_{COD} <0. In conclusion, for the dry tilted penny-shaped crack permeating in the VTI background, when $\Delta^{H}_{COD} < 0$, the COD tensor in the *xyz* system can be approximately estimated by $\mathbf{B}^{hor}$, that is,

$$\mathbf{B}^{b} \approx \mathbf{B}^{hor}; \tag{15}$$

when Δ^{H}_{COD} >0, the COD tensor in the $x'y'z'$ system is very close to $\mathbf{B}^{hor}$ so that $\mathbf{B}^{n} \approx \mathbf{B}^{hor}$. Using Eq. (11), the approximation of $\mathbf{B}^{n}$ can be further transformed into the COD tensor in the *xyz* system, namely

$$\mathbf{B}^{b} = \mathbf{L}\mathbf{B}^{n}\mathbf{L}^{T} \approx \mathbf{L}\mathbf{B}^{hor}\mathbf{L}^{T} = \begin{bmatrix} B^{hor}_{11} & 0 & 0 \\ 0 & B^{b}_{22} & B^{b}_{23} \\ 0 & B^{b}_{23} & B^{b}_{33} \end{bmatrix}, \tag{16}$$

where $B^{b}_{22} = \cos^2\zeta B^{hor}_{11} + \sin^2\zeta B^{hor}_{33}$, $B^{b}_{33} = \sin^2\zeta B^{hor}_{11} + \cos^2\zeta B^{hor}_{33}$, $B^{b}_{23} = \cos\zeta \sin\zeta (B^{hor}_{33} - B^{hor}_{11})$.

To further verify the above conclusion, Eqs. (15) and (16) are utilized to estimate COD tensors of dry tilted cracks in forty groups of VTI backgrounds, respectively, and errors of the estimations are measured by

$$\Lambda^{**}_{ij}(\zeta) = \left|B^{**}_{ij}(\zeta) - B_{ij}(\zeta)\right| \Big/ B_{ij}(\zeta) \quad (i, j = 1, 2, 3). \tag{17}$$

In Eq. (17), $B_{ij}(\zeta)$ denotes the accurate COD tensor of the crack with the dip angle of ζ, which is calculated with Eqs. (3) and (4). $B^{**}_{ij}(\zeta)$ is the corresponding estimation. $\Lambda^{**}_{ij}(\zeta)$ represents the error of the estimation. Fig. 9 shows the maximums of $\Lambda^{**}_{ii}(\zeta)$ with respect to the dip angle ζ for forty VTI background cases. Fig. 9a reveals that the estimations of the 1st diagonal element from Eqs. (15) and (16) have equal accuracy. We also find that the blue pentagrams in Fig. 9b and c match with those in Fig. 8 well with the exception of the 27th sample. Therefore, the estimation from Eq. (15) is optimal for the case with Δ^{H}_{COD} <0, and the estimation from Eq. (16) is better for the case with Δ^{H}_{COD} >0, which well verifies the previous conclusion. For the 27th VTI background, the value of g is 0.54, which leads to $\Delta^{H}_{COD}\big|_{\varepsilon,\gamma,\delta=0} < 0$. Fig. 2b and c implies that B^{hor}_{22} and B^{hor}_{33} increase with the decreasing anisotropic parameters ε and γ and the increasing rate of B^{hor}_{22} is larger than that of B^{hor}_{33}. Consequently, the negative anisotropic parameters ε and γ of the 27th VTI background cause the change of the sign of Δ^{H}_{COD}, that is, $\Delta^{H}_{COD} > 0$ (as seen in Fig. 8), which suggests the background anisotropy becomes the main influence on the CODs. Hence, Eq. (15) is better for estimating the COD tensor of the crack in the 27th VTI background (as in Fig. 9), although $\Delta^{H}_{COD} > 0$. The finding from the 27th case is contrary to that from other 39 cases, but the rock with $g > 0.5$ and negative anisotropic parameters ε and γ is extremely infrequent underground. Therefore, the conclusion from other 39 cases expounded by Eqs. (15) and (16) has wider applicability.

Integrating Eqs. (15) and (16), we can approximately derive the final analytical solution of the COD tensor of the dry inclined circular crack in the VTI background as

$$\boldsymbol{B} = \begin{bmatrix} B_{11} & 0 & 0 \\ 0 & B_{22} & B_{23} \\ 0 & B_{23} & B_{33} \end{bmatrix}, \tag{18}$$

where $B_{11} = B^{hor}_{11}$, $B_{22} = B^{hor}_{11} + \lambda_n\left(B^{hor}_{33} - B^{hor}_{11}\right)\sin^2\zeta$, $B_{33} = B^{hor}_{33} + \lambda_n\left(B^{hor}_{11} - B^{hor}_{33}\right)\sin^2\zeta$, and $B_{23} = \lambda_n\left(B^{hor}_{33} - B^{hor}_{11}\right)\sin\zeta\cos\zeta$. In Eq. (18), $\lambda_n = 1$ for $\Delta^{H}_{COD} > 0$, and $\lambda_n = 0$ for $\Delta^{H}_{COD} < 0$. Note that Eq. (18) is the expression in the *xyz* system.

2.3. Effective elastic properties for the rock with a tilted set of penny-shaped cracks in the VTI background

Rotation of the crack around the z axis cannot change the effective elastic properties of the rock with a tilted set of penny-shaped cracks in the VTI background. Hence, we set the angle between the y axis and the projection of the symmetry axis of the crack onto the *xoy* plane to zero degree. As shown in Fig. 1b, the unit direction vector of the symmetry axis of the crack

$$\mathbf{n} = (0, \sin\zeta, \cos\zeta). \tag{19}$$

Substituting Eqs. (18) and (19) into Eq. (4), the compliance contribution matrix $\mathbf{H}_c$ of an aligned set of dry tilted penny-shaped cracks embedded in the VTI background can be expressed in the form of the Voigt's concise notation, namely

$$\mathbf{H}_c = \frac{\pi e}{a}\sin\zeta\cos\zeta\times$$

$$\begin{bmatrix} 0 & 0 & 0 & 0 & 0 & 0 \\ 0 & B_{22}\tan\zeta & B_{23} & B_{22}+B_{23}\tan\zeta & 0 & 0 \\ 0 & B_{23} & B_{33}\cot\zeta & B_{33}+B_{23}\cot\zeta & 0 & 0 \\ 0 & B_{22}+B_{23}\tan\zeta & B_{33}+B_{23}\cot\zeta & B_{22}\cot\zeta+B_{33}\tan\zeta+2B_{23} & 0 & 0 \\ 0 & 0 & 0 & 0 & B_{11}\cot\zeta & B_{11} \\ 0 & 0 & 0 & 0 & B_{11} & B_{11}\tan\zeta \end{bmatrix}, \tag{20}$$

where $\cot\zeta = (\tan\zeta)^{-1}$. Eq. (20) ignores effects of the elastic interactions between cracks on effective properties, which is applicable to the case for the rock containing dilute concentration of cracks. Hence, the effective compliance matrix $\mathbf{S}_{\text{eff}}$ of the overall rock is

$$\mathbf{S}_{\text{eff}} = \mathbf{S}^0 + \mathbf{H}_c. \tag{21}$$

The compliance matrix $\mathbf{S}^0$ of the VTI background is the inverse of the stiffness matrix $\mathbf{C}^0$, namely

$$\mathbf{S}^0 = \left(\mathbf{C}^0\right)^{-1} = \begin{bmatrix} \mathbf{S}_1^0 & \mathbf{0} \\ \mathbf{0} & \mathbf{S}_2^0 \end{bmatrix}, \tag{22}$$

where

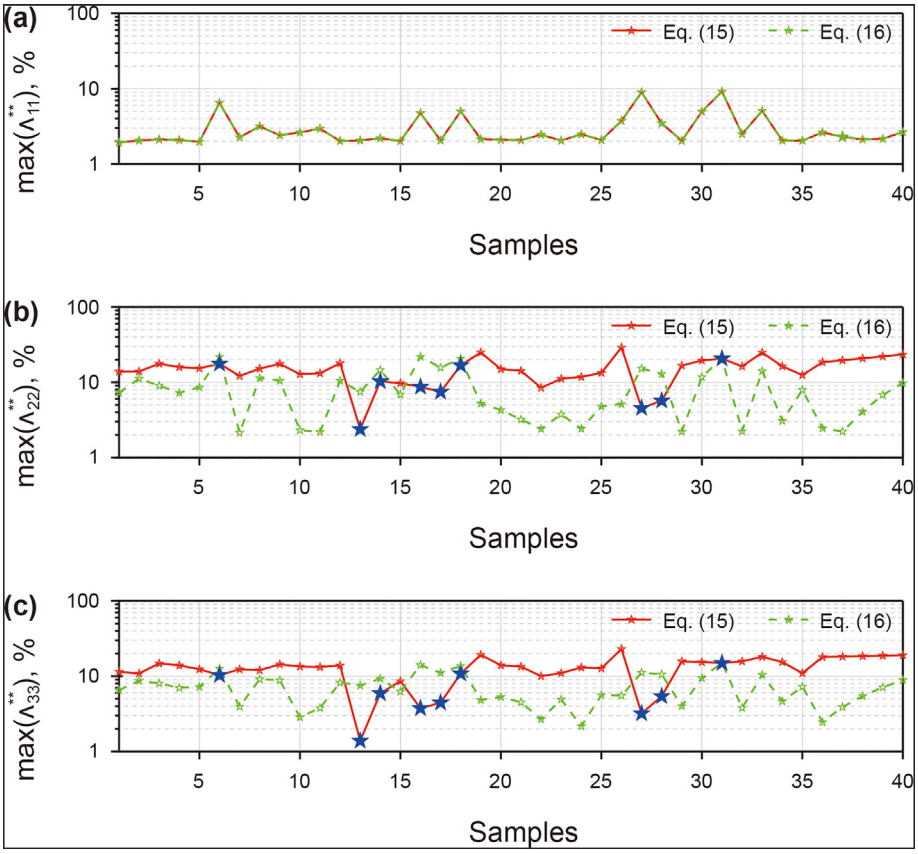

Fig. 9. Maximum errors of the estimations of the (a) 1st, (b) 2nd and (c) 3rd diagonal elements of the COD tensors of the dry crack in forty VTI backgrounds with respect to the dip angle. The red and green lines indicate the maximum errors of the estimations from Eqs. (15) and (16), respectively. The blue pentagram signifies the maximum error of Eq. (15) is less than that of Eq. (16). Note the *y*-axis is the logarithmic axis.

$$\mathbf{S}_1^0 = \frac{1}{4}\begin{bmatrix} 2c_{33}^0/c + 1/c_{66}^0 & 2c_{33}^0/c - 1/c_{66}^0 & -4c_{13}^0/c \\ 2c_{33}^0/c - 1/c_{66}^0 & 2c_{33}^0/c + 1/c_{66}^0 & -4c_{13}^0/c \\ -4c_{13}^0/c & -4c_{13}^0/c & 4(c_{11}^0 + c_{12}^0)/c \end{bmatrix}, \quad \mathbf{S}_2^0 = \begin{bmatrix} 1/c_{44}^0 & 0 & 0 \\ 0 & 1/c_{44}^0 & 0 \\ 0 & 0 & 1/c_{66}^0 \end{bmatrix}$$

and $c = c_{33}^0(c_{11}^0 + c_{12}^0) - 2(c_{13}^0)^2$. Likewise, the effective stiffness matrix $\mathbf{S}_{\text{eff}}$ of the overall rock can be obtained by inverting the effective compliance matrix $\mathbf{S}_{\text{eff}}$.

Brown and Korringa (1975) published a fluid substitution equation for an anisotropic medium, which can be written as

$$\mathbf{S}_{\text{eff}}^{\text{sat}} = \mathbf{S}^0 + \mathbf{H}_{\text{c}} + \mathbf{F}. \tag{23}$$

For this equation, $\mathbf{S}_{\text{eff}}^{\text{sat}}$ is the effective compliance matrix of the saturated rock. The matrix $\mathbf{F}$ represents the compliance change caused by the fluid filling cracks. Substituting Eqs. (20)–(22) into Eq. (23) and taking the inverse of the result yields the elastic stiffness matrix of the saturated rock. If the background anisotropy is induced by the horizontally oriented fractures, the cracks will be hydraulically connected with the horizontal fractures. Huang et al. (2015) has investigated the effects of the pore fluid on elastic properties and seismic responses of the saturated rock for this case. If the VTI background is formed by the aligned arrangement or crystal lattice of minerals, such as shale, and the porosity of the background is very low, the tilted cracks may be hydraulically connected with each other but isolated from the background matrix. For the sake of simplicity, we focus on the impacts of the fluid on the elastic responses of the rock in the second case. Whereupon, the ij component of the compliance change matrix $\mathbf{F}$ can be specifically written as

$$F_{ij} = -\frac{\sum_{a=1}^{3} h_{c_{ia}} \sum_{b=1}^{3} h_{c_{bj}}}{\sum_{p=1}^{3}\sum_{q=1}^{3} h_{c_{pq}} + \varphi_{\text{c}}\left(1/K_{\text{f}} - 1/K_{\text{g}}\right)} \quad (i, j = 1, 2, 3, 4, 5, 6), \tag{24}$$

where K_{f} is the bulk modulus of the fluid and $h_{c_{pq}}$ is the pq element of the compliance contribution matrix of the dry cracks. And $K_{\text{g}} = c/(c_{11}^0 + c_{12}^0 + 2c_{33}^0 - 4c_{13}^0)$.

For the case of the horizontal cracks, $\zeta = 0^\circ$ and the compliance contribution matrix of the dry cracks can be simplified as

$$\mathbf{H}_{\text{c}}^{\text{hor}} = \begin{bmatrix} 0 & 0 & 0 & 0 & 0 & 0 \\ 0 & 0 & 0 & 0 & 0 & 0 \\ 0 & 0 & Z_{\text{N}}^{\text{hor}} & 0 & 0 & 0 \\ 0 & 0 & 0 & Z_{\text{T}}^{\text{hor}} & 0 & 0 \\ 0 & 0 & 0 & 0 & Z_{\text{T}}^{\text{hor}} & 0 \\ 0 & 0 & 0 & 0 & 0 & 0 \end{bmatrix}, \tag{25}$$

where the superscript 'hor' means the horizontal cracks. The symbols Z_{N} and Z_{T} denote the normal and tangential compliance parameters of the cracks, respectively, and

$$Z_{\text{N}}^{\text{hor}} = \frac{\pi e}{a} B_{33}^{\text{hor}}, \tag{26}$$

$$Z_{\text{T}}^{\text{hor}} = \frac{\pi e}{a} B_{11}^{\text{hor}}. \tag{27}$$

Obviously, Eqs. (26) and (27) are independent of λ_{n}. Substituting Eqs. (22) and (25) into Eq. (21) and taking the inverse of the result yields

$$\mathbf{C}_{\text{eff}}^{\text{hor}} = \mathbf{C}^0 + \mathbf{C}_{\text{c}}^{\text{hor}}, \tag{28}$$

where the stiffness contribution matrix induced by the horizontal cracks is

$$\mathbf{C}_{\text{c}}^{\text{hor}} = -\begin{bmatrix} \frac{(c_{13}^0)^2}{c_{33}^0}\Delta_{\text{N}}^{\text{hor}} & \frac{(c_{13}^0)^2}{c_{33}^0}\Delta_{\text{N}}^{\text{hor}} & c_{13}^0\Delta_{\text{N}}^{\text{hor}} & 0 & 0 & 0 \\ \frac{(c_{13}^0)^2}{c_{33}^0}\Delta_{\text{N}}^{\text{hor}} & \frac{(c_{13}^0)^2}{c_{33}^0}\Delta_{\text{N}}^{\text{hor}} & c_{13}^0\Delta_{\text{N}}^{\text{hor}} & 0 & 0 & 0 \\ c_{13}^0\Delta_{\text{N}}^{\text{hor}} & c_{13}^0\Delta_{\text{N}}^{\text{hor}} & c_{33}^0\Delta_{\text{N}}^{\text{hor}} & 0 & 0 & 0 \\ 0 & 0 & 0 & c_{44}^0\Delta_{\text{T}}^{\text{hor}} & 0 & 0 \\ 0 & 0 & 0 & 0 & c_{44}^0\Delta_{\text{T}}^{\text{hor}} & 0 \\ 0 & 0 & 0 & 0 & 0 & 0 \end{bmatrix}. \tag{29}$$

In Eq. (29), Δ_{N} and Δ_{T} are named the normal and tangential weakness parameters, respectively, and

$$\Delta_{\text{N}}^{\text{hor}} = \frac{c_{33}^0 Z_{\text{N}}^{\text{hor}}}{1 + c_{33}^0 Z_{\text{N}}^{\text{hor}}}, \tag{30}$$

$$\Delta_{\text{T}}^{\text{hor}} = \frac{c_{44}^0 Z_{\text{T}}^{\text{hor}}}{1 + c_{44}^0 Z_{\text{T}}^{\text{hor}}}. \tag{31}$$

Substituting Eq. (25) into (24), all components of the excess compliance matrix $\mathbf{F}$ equal zero with the exception of

$$F_{33}^{\text{hor}} = -\frac{\left(Z_{\text{N}}^{\text{hor}}\right)^2}{Z_{\text{N}}^{\text{hor}} + \varphi_{\text{c}}\left(1/K_{\text{f}} - 1/K_{\text{g}}\right)}. \tag{32}$$

In consequence, the normal and tangential compliance parameters of the saturated cracks, namely $Z_{\text{N}}^{\text{hor\_sat}}$ and $Z_{\text{T}}^{\text{hor\_sat}}$, can be defined as

$$Z_{\mathrm{N}}^{\mathrm{hor\_sat}} = Z_{\mathrm{N}}^{\mathrm{hor}} + F_{33}^{\mathrm{hor}}, \tag{33}$$

$$Z_{\mathrm{T}}^{\mathrm{hor\_sat}} = Z_{\mathrm{T}}^{\mathrm{hor}}. \tag{34}$$

Substituting $Z_{\mathrm{N}}^{\mathrm{hor\_sat}}$ for $Z_{\mathrm{N}}^{\mathrm{hor}}$ in Eqs. (28)–(30), we can derive the effective stiffness matrix $\mathbf{C}_{\mathrm{eff}}^{\mathrm{hor\_sat}}$ of the saturated rock.

For the case of the vertical cracks, $\zeta = 90^{\circ}$ and the compliance contribution matrix of the dry cracks can be simplified as

$$\mathbf{H}_{\mathrm{c}}^{\mathrm{ver}} = \begin{bmatrix} 0 & 0 & 0 & 0 & 0 & 0 \\ 0 & Z_{\mathrm{N}}^{\mathrm{ver}} & 0 & 0 & 0 & 0 \\ 0 & 0 & 0 & 0 & 0 & 0 \\ 0 & 0 & 0 & Z_{\mathrm{V}}^{\mathrm{ver}} & 0 & 0 \\ 0 & 0 & 0 & 0 & 0 & 0 \\ 0 & 0 & 0 & 0 & 0 & Z_{\mathrm{H}}^{\mathrm{ver}} \end{bmatrix}, \tag{35}$$

where the superscript 'ver' signifies the vertical crack case. The symbols Z_{V} and Z_{H} represent the vertical and horizontal compliance parameters, respectively, and

$$Z_{\mathrm{N}}^{\mathrm{ver}} = \frac{\pi e}{a}\left[(1-\lambda_{\mathrm{n}})B_{11}^{\mathrm{hor}} + \lambda_{\mathrm{n}} B_{33}^{\mathrm{hor}}\right], \tag{36}$$

$$Z_{\mathrm{V}}^{\mathrm{ver}} = \frac{\pi e}{a}\left[\lambda_{\mathrm{n}} B_{11}^{\mathrm{hor}} + (1-\lambda_{\mathrm{n}})B_{33}^{\mathrm{hor}}\right], \tag{37}$$

$$Z_{\mathrm{H}}^{\mathrm{ver}} = \frac{\pi e}{a} B_{11}^{\mathrm{hor}}. \tag{38}$$

Substituting Eqs. (22) and (35) into Eq. (21) and taking the inverse of the result gives

$$\mathbf{C}_{\mathrm{eff}}^{\mathrm{ver}} = \mathbf{C}^{0} + \mathbf{C}_{\mathrm{c}}^{\mathrm{ver}}, \tag{39}$$

where the stiffness contribution matrix induced by the vertical cracks is

$$\mathbf{C}_{\mathrm{c}}^{\mathrm{ver}} = -\begin{bmatrix} \frac{\left(c_{12}^{0}\right)^{2}}{c_{11}^{0}}\Delta_{\mathrm{N}}^{\mathrm{ver}} & c_{12}^{0}\Delta_{\mathrm{N}}^{\mathrm{ver}} & \frac{c_{12}^{0}c_{13}^{0}}{c_{11}^{0}}\Delta_{\mathrm{N}}^{\mathrm{ver}} & 0 & 0 & 0 \\ c_{12}^{0}\Delta_{\mathrm{N}}^{\mathrm{ver}} & c_{11}^{0}\Delta_{\mathrm{N}}^{\mathrm{ver}} & c_{13}^{0}\Delta_{\mathrm{N}}^{\mathrm{ver}} & 0 & 0 & 0 \\ \frac{c_{12}^{0}c_{13}^{0}}{c_{11}^{0}}\Delta_{\mathrm{N}}^{\mathrm{ver}} & c_{13}^{0}\Delta_{\mathrm{N}}^{\mathrm{ver}} & \frac{\left(c_{13}^{0}\right)^{2}}{c_{11}^{0}}\Delta_{\mathrm{N}}^{\mathrm{ver}} & 0 & 0 & 0 \\ 0 & 0 & 0 & c_{44}^{0}\Delta_{\mathrm{V}}^{\mathrm{ver}} & 0 & 0 \\ 0 & 0 & 0 & 0 & 0 & 0 \\ 0 & 0 & 0 & 0 & 0 & c_{66}^{0}\Delta_{\mathrm{H}}^{\mathrm{ver}} \end{bmatrix}. \tag{40}$$

In Eq. (40), Δ_{V} and Δ_{H} are named the vertical and horizontal weakness parameters, respectively, and

$$\Delta_{\mathrm{N}}^{\mathrm{ver}} = \frac{c_{11}^{0} Z_{\mathrm{N}}^{\mathrm{ver}}}{1 + c_{11}^{0} Z_{\mathrm{N}}^{\mathrm{ver}}}, \tag{41}$$

$$\Delta_{\mathrm{V}}^{\mathrm{ver}} = \frac{c_{44}^{0} Z_{\mathrm{V}}^{\mathrm{ver}}}{1 + c_{44}^{0} Z_{\mathrm{V}}^{\mathrm{ver}}}, \tag{42}$$

$$\Delta_{\mathrm{H}}^{\mathrm{ver}} = \frac{c_{66}^{0} Z_{\mathrm{H}}^{\mathrm{ver}}}{1 + c_{66}^{0} Z_{\mathrm{H}}^{\mathrm{ver}}}. \tag{43}$$

Similar to the horizontal crack case, substituting Eq. (35) into Eq. (24) gives the matrix in which all elements equal zero except

$$F_{22}^{\mathrm{ver}} = -\frac{\left(Z_{\mathrm{N}}^{\mathrm{ver}}\right)^{2}}{Z_{\mathrm{N}}^{\mathrm{ver}} + \varphi_{\mathrm{c}}\left(1/K_{\mathrm{f}} - 1/K_{\mathrm{g}}\right)}. \tag{44}$$

Thereupon, the compliance parameters of the vertical saturated crack can be defined as

$$Z_{\mathrm{N}}^{\mathrm{ver\_sat}} = Z_{\mathrm{N}}^{\mathrm{ver}} + F_{22}^{\mathrm{ver}}, \tag{45}$$

$$Z_{\mathrm{V}}^{\mathrm{ver\_sat}} = Z_{\mathrm{V}}^{\mathrm{ver}}. \tag{46}$$

$$Z_{\mathrm{H}}^{\mathrm{ver\_sat}} = Z_{\mathrm{H}}^{\mathrm{ver}}. \tag{47}$$

As a result, we can derive the effective stiffness matrix $\mathbf{C}_{\mathrm{eff}}^{\mathrm{ver\_sat}}$ of the saturated rock by replacing $Z_{\mathrm{N}}^{\mathrm{ver}}$ in Eqs. (39)–(41) with $Z_{\mathrm{N}}^{\mathrm{ver\_sat}}$.

3. Numerical cases

3.1. Parameters

For the cracked medium as shown in Fig. 1b, the velocities propagating in the y-z plane reflect not only the anisotropy induced by the aligned cracks, but also the anisotropy caused by the VTI background. Therefore, a numerical model is designed to analyze the effects of the background anisotropy, filled fluid, crack dip angle, and crack density on the effective elastic properties of the cracked medium and the P- and S-wave velocities traveling in the y-z plane. Parameters of a tight sand sample with a relatively high degree of VTI anisotropy, $c_{11}^{0} = 47.31$ GPa, $c_{33}^{0} = 33.89$ GPa, $c_{12}^{0} = 7.83$ GPa, $c_{13}^{0} = 5.29$ GPa, $c_{44}^{0} = 17.15$ GPa and the mass density $\rho = 2.504$ g/cm^3, utilized by Guo et al. (2019) are introduced in order to better compare the results in this paper with those given by Guo et al. (2019). Unless otherwise specified, aligned cracks with the crack density of 0.05 and the aspect ratio of 0.001 are added into the VTI background to simulate the cracked rock. And the effect of the aligned cracks on the mass density of the overall medium is negligible and then the mass density of the cracked medium can be assumed to be 2.504 g/cm^3. The bulk modulus of the fluid filling the cracks is 2.5 GPa. Dry and saturated effective stiffness parameters of the designed cracked rock can be estimated by taking the inverse of the results of Eqs. (21) and (23), respectively. The phase velocities of the P and S waves can be calculated by Eqs. (B-1)–(B-4) in Appendix B. Meanwhile, a cracked rock with the isotropic background that has the stiffness parameters $c_{11}^{0} = 47.31$ GPa and $c_{12}^{0} = 7.83$ GPa is also designed as a reference medium using the above method.

3.2. Effects of crack dip angle, background anisotropy and fluid

Fig. 10 demonstrates the nine stiffness coefficients of the

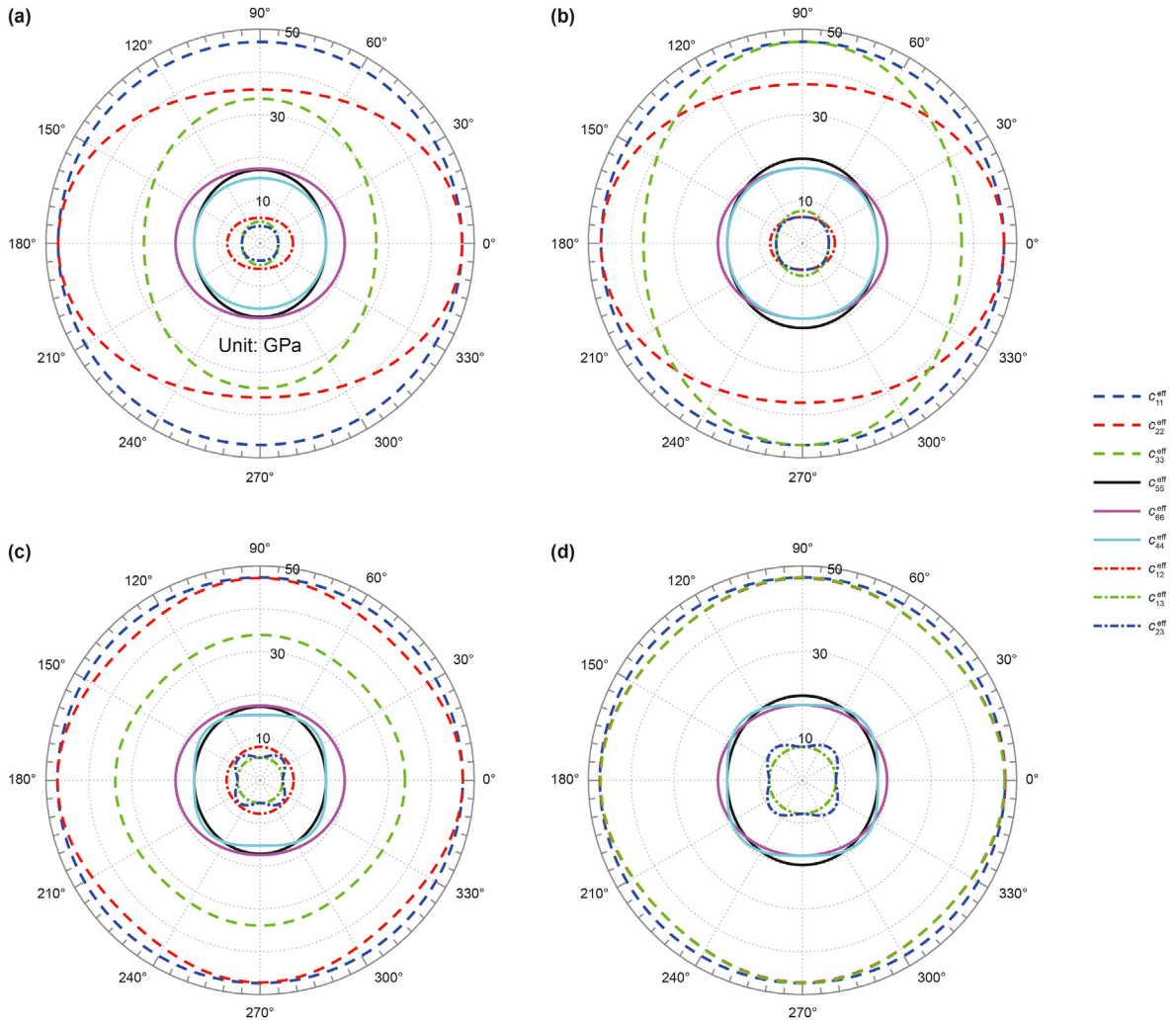

Fig. 10. Variations of stiffness coefficients of the cracked media with the crack dip angle. The rocks contain dry cracks in the (a) VTI and (b) isotropic backgrounds, respectively. The rocks contain saturated cracks in the (c) VTI and (d) isotropic backgrounds, respectively.

cracked media varing with the crack dip angle because other coefficients are either zero or much smaller than these nine coefficients and are thus not analyzed. For the dry cracked rock, Fig. 10a and b shows that c_{11}^{eff} is nearly independent of the crack dip angle regardless of the degree of the background anisotropy. With the increase of the crack dip angle from 0° to 90°, c_{22}^{eff} and c_{66}^{eff} gradually decrease, and c_{33}^{eff} and c_{55}^{eff} monotonously increase whether the background is anisotropic or isotropic. And c_{44}^{eff} is slightly dependent on the crack dip angle. These variations can be explained by the fact that stiffness coefficients of the rock are functions of reciprocals of corresponding compliance coefficients according to the formula of matrix inversion. The variations of the stiffness coefficients with the crack dip angle are basically consistent with those of the reciprocals of the corresponding compliance parameters. According to Eqs. (20) and (21), the element s_{11}^{eff} is not affected by the aligned cracks. Hence, the reciprocal of s_{11}^{eff} is unrelated to the crack dip angle. The reciprocals of s_{22}^{eff} and s_{66}^{eff} are both functions of $\sin^{-2}\zeta$ and the reciprocals of s_{33}^{eff} and s_{55}^{eff} are both functions of $\cos^{-2}\zeta$. The functions $\sin^{-2}\zeta$ and $\cos^{-2}\zeta$ are monotonically decreasing and increasing functions within the range of the dip angle from 0° to 90°, respectively. The dependence of s_{44}^{eff} on the dip angle is determined by $\left|B_{33}^{\text{hor}} - B_{11}^{\text{hor}}\right|$. From Fig. 2, we can conclude that the value of $\left|B_{33}^{\text{hor}} - B_{11}^{\text{hor}}\right|$ is smaller than that of B_{11}^{hor} for most cases so that the reciprocal of s_{44}^{eff} is weakly dependent on the dip angle. Fig. 10a and b also illustrates that variations of c_{12}^{eff} and c_{13}^{eff} with the crack dip angle are similar to those of c_{22}^{eff} and c_{33}^{eff}, respectively. Moreover, c_{23}^{eff} is weakly dependent on the crack dip angle. These are due to that the off-diagonal elements of the stiffness contribution matrix represent the coupled information of the diagonal elements, for example, $\left|c_{c12}^{\text{hor}}\right|$ in matrix (29) is equal to the square root of c_{c11}^{hor} multiplying c_{c22}^{hor}. Background parameters are independent of the crack dip angle so that the variation of the off-diagonal effective stiffness parameter with the crack dip angle is a coupled response of those of the corresponding diagonal parameters. Furthermore, c_{11}^{eff} has extremely weak dependence on the crack dip angle. Therefore, variations of c_{12}^{eff} and c_{13}^{eff} with the crack dip angle are similar to those of c_{22}^{eff} and c_{33}^{eff}, respectively. The change of c_{22}^{eff} with the crack dip angle is opposite to that of c_{33}^{eff} and in consequence, c_{23}^{eff} is weakly dependent on the crack dip angle.

According to Eqs. (B−1) and (B−3), the velocities of the P waves

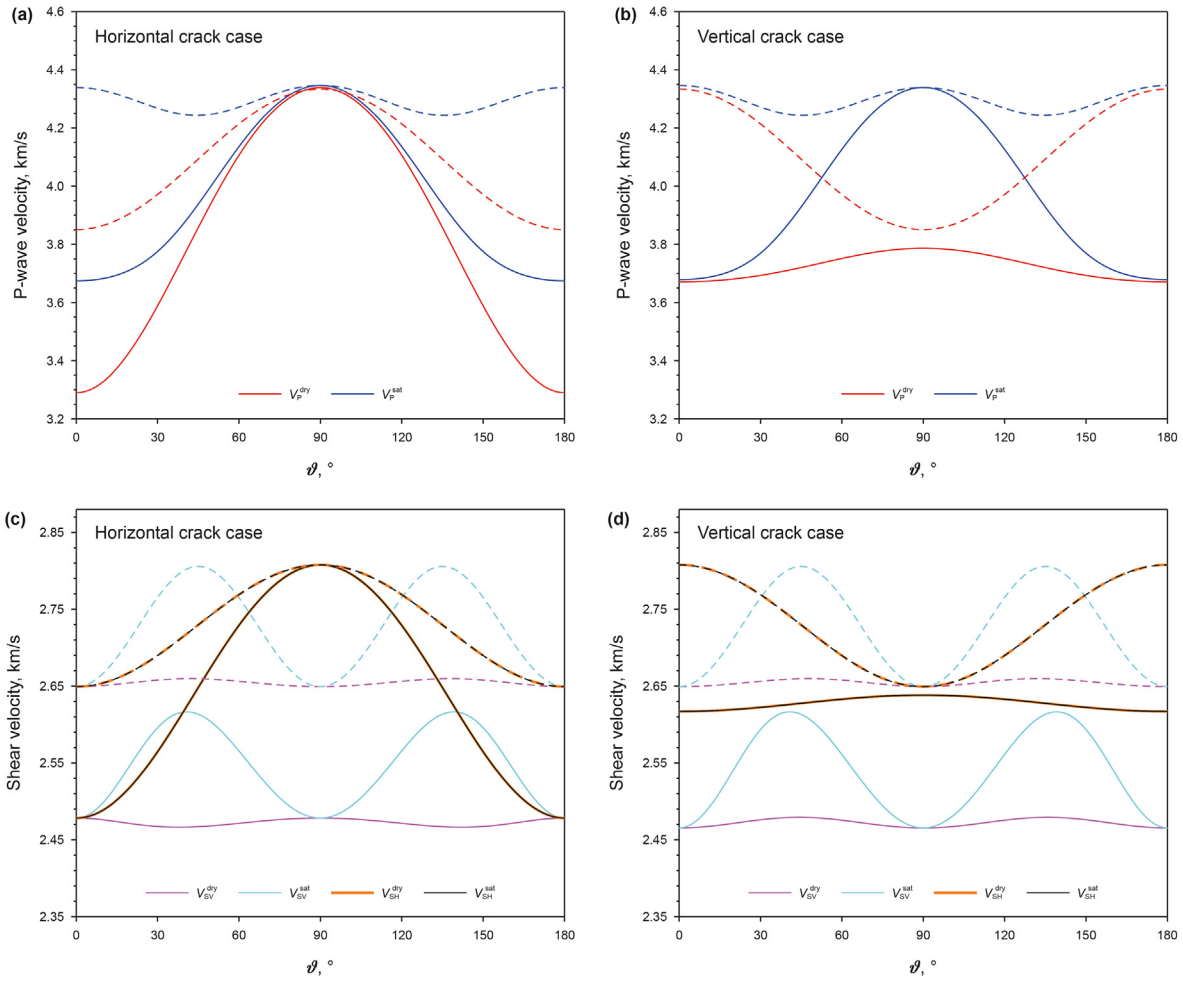

Fig. 11. Variations of P-, SV- and SH-wave phase velocities with the incident angle ϑ. Figures (a) and (c) correspond to the horizotal crack case, and Figures (b) and (d) the vertical crack case. The dashed and solid lines represent the isotropic and VTI backgrounds cases, respectively. Superscripts 'dry' and 'sat' denote the dry and saturated rocks, respectively.

vertically ($\vartheta = 0°$, where ϑ represents the angle between the incident direction and the z-axis) and horizontally ($\vartheta = 90°$) propagating in the y-z plane are determined by c_{33}^{eff} and c_{22}^{eff}, respectively. The velocities of the SH waves vertically and horizontally propagating are determined by c_{55}^{eff} and c_{66}^{eff}, respectively. Hence, the variations of the stiffness coefficients as analyzed above will cause increases of the vertical P- and SH-wave velocities and decreases of the horizontal P- and SH-wave velocities with the increasing crack dip angle. In order to illustrate these more clearly, Fig. 11 shows the phase velocities changing with the incident angle ϑ for the cases with horizontal and vertical cracks, respectively. We can obviously observe the larger vertical P- and SH-wave velocities and the smaller horizontal P- and SH-wave velocities for the dry vertical crack case than for the dry horizontal crack case. It can be further inferred that the increase of the dip angle may make the P-wave velocity anisotropy decrease to zero first, and then increase inversely. The specific change of the P-wave velocity anisotropy is related to the degree of background anisotropy. The effect of the dip angle on the SH-wave velocity anisotropy is similar to that of the P wave. These indicate the great influence of the crack dip angle. Additionally, for the SV-wave velocity of the dry crack case, Fig. 11c and d demonstrates that its change with the crack dip angle is relatively small. However, its trends with the incident angle ϑ are opposite for two cases of the horizontal cracks and the vertical cracks in the VTI background. For the case of the horizontal cracks in the VTI background, the SV-wave velocity minimizes when $\vartheta \approx 45°$ or 135°, whereas it peaks at these incident angles for the case of the vertical cracks. This is due to that the background anisotropy is approximate elliptical (namely $\varepsilon \approx \delta$) so that similar to that in an isotropic medium, the SV-wave velocity in the VTI background medium is nearly independent of the incident angle. It causes that properties of the aligned cracks control the trend of the SV-wave velocity with the incident angle. Eqs. (28), (39) and (B-2) disclose that the SV-wave velocity at the 0° incident angle principally depends on the vertical compliance Z_V, while that at the 45° incident angle is mainly influenced by the normal compliance Z_N. The smaller values of Z_V and Z_N induce the bigger SV-wave velocities at the incident angles of 0° and 45°, respectively. Consequently, the relative value between Z_N and Z_V determines the variation of the SV-wave velocity with the incident angle. For the case of the horizontal cracks in the VTI background, Z_N (0.0074 GPa^{-1}) is slightly bigger than Z_V (also called Z_T, 0.0067 GPa^{-1}) so that the SV-wave velocity at the 45° incident angle is slightly smaller than that at the 0° incident angle. For the case of the vertical cracks in the VTI background, Z_N (0.0067 GPa^{-1}) is slightly smaller than Z_V (0.0074 GPa^{-1}), which leads to the reverse variation of the SV-wave velocity with the incident angle. Besides, for the two cases of the horizontal and vertical cracks in the isotropic background, the SV-wave velocities at the 45° incident angle should be equal to each other. The values of c_{44}^{eff} should also be the same as each other,

which determine the SV-wave velocities at the incident angle of 0° or 90°. In consequence, the trends of the SV-wave velocities with the incident angle should be similar to each other for the two cases, as shown by the magenta dashed lines in Fig. 11c and d. However, Guo et al. (2019) gave reverse trends of the SV-wave velocities with the incident angle for the two cases (as shown by green dashed lines in Figs. 4b and 8b of Guo et al. (2019)). Moreover, for the case of the vertical cracks in the isotropic background, c_{44}^{eff} should be equal to c_{66}^{eff}. Hence, according to Eqs. (B-2) and (B-3), the SH-wave velocity (the saffron dashed line in Fig. 11d) is equal to the SV-wave velocity (the magenta dashed line in Fig. 11d) when the incident angle reaches 90°. Nevertheless, the blue and green dashed lines in Fig. 8b of Guo et al. (2019) show that these two velocities are different at the 90° incident angle. These suggest that the solution proposed in this paper is more reasonable than that given by Guo et al. (2019) for the case with a weakly anisotropic background.

By comparing Fig. 10a with 10b, it can be found that substitution of the VTI background for the isotropic background has little effects on c_{11}^{eff}, c_{22}^{eff} and c_{66}^{eff} with the exception of a little smaller c_{22}^{eff} and c_{66}^{eff} for the vertical cracks case. This is owing to the fact that the VTI background has the same c_{11}^{0} and c_{66}^{0} as the isotropic background. Eqs. (29) and (40) reveal that c_{22}^{eff} and c_{66}^{eff} of the horizontal cracks case and c_{11}^{eff} have very small sensitivities on the crack compliance parameters. Therefore, they are nearly constant with the background medium varying from the isotropic medium to the anisotropic medium. For the vertical cracks case, the increasing degrees of the background anisotropy cause the increases of Z_{N} (from 0.0058 GPa^{-1} to 0.0067 GPa^{-1}) and Z_{H} (from 0.0062 GPa^{-1} to 0.0067 GPa^{-1}) and hence, c_{22}^{eff} and c_{66}^{eff} of the VTI background case are smaller than those of the isotropic background case according to Eqs. (39) and (40). Additionally, c_{33}^{0}, c_{44}^{0} and c_{55}^{0} gradually decrease with the increases of the background anisotropic parameters ε and γ. In consequence, c_{33}^{eff}, c_{44}^{eff} and c_{55}^{eff} are smaller for the VTI background case than for the isotropic background case according to Eqs. (28) and (39), as shown in Fig. 10a and b. Moreover, with substituting the VTI background for the isotropic background, c_{13}^{eff} and c_{23}^{eff} will also be lower owing to the decrease of c_{33}^{eff}, while c_{12}^{eff} is hardly affected due to very weak changes in c_{11}^{eff} and c_{22}^{eff}.

These changes in the effective stiffness coefficients will lead to changes in the phase velocities, as shown in Fig. 11. For the dry horizontal cracks case (Fig. 11a and c), as the degree of the background anisotropy increases, both the P- and SH-wave velocities at the normal incidence decrease and both the velocities at the incident angle of 90° are almost constant. Thus, the VTI background can enhance the degrees of the P- and SH-wave velocities anisotropy, which are consistent with the experiment results given by Ding et al. (2017, Figs. 7–10). Fig. 11c also reveals that existence of the VTI background not only reduces the SV-wave velocity, but also changes the trend of the SV-wave velocity with the incident angle. This is due to that existence of the VTI background not only reduces c_{44}^{eff}, but changes the relative value between Z_{N} and Z_{T}. For the vertical cracks case (Fig. 11b and d), the VTI background reduces both the vertical and horizontal P-wave velocities, but the horizontal velocity decreases less. The change of the SH-wave velocity is similar to that of the P-wave velocity. Therefore, we can infer that the anisotropies of the P- and SH-wave velocities decrease first and then increase with the increasing degrees of the background anisotropy, which are similar to experiment results given by Silva et al. (2019, Figs. 5 and 6). From Fig. 11d, it can be seen that existence of the VTI background makes the SV-wave velocity decrease owing to smaller c_{44}^{eff}.

When the aligned cracks are saturated with fluid, variations of the nine stiffness coefficients with the crack dip angle are shown in Fig. 10c and d. For the two cases of the horizontal and vertical cracks, it can be seen from Fig. 10c and d that fluid saturation makes the elements related to the compressional moduli (namely c_{11}^{eff}, c_{22}^{eff}, c_{33}^{eff}, c_{12}^{eff}, c_{13}^{eff} and c_{23}^{eff}) larger and has no effects on the shear moduli (c_{44}^{eff}, c_{55}^{eff} and c_{66}^{eff}). This results from that fluid saturation reduces the value of Z_{N}, whereas does not change the values of Z_{V} and Z_{H} (or Z_{T}), as given by Eqs. (33), (34) and (45)–(47). Thus, the stiffness coefficients related to Z_{N} will be bigger and the shear moduli related to Z_{T} will be constant according to Eqs. (29) and (40). The increases of the compressional moduli induce the bigger P-wave velocities (blue lines in Fig. 11a and b) and the bigger SV-wave velocities at the incident angles of around 45° and 135° (cyan lines in Fig. 11c and d). The constant shear moduli cause no changes of the SH-wave velocities (black lines in Fig. 11c and d) and the SV-wave velocities at the incident angles of 0° and 90°. Furthermore, c_{22}^{eff} of the horizontal cracks case, c_{33}^{eff} of the vertical cracks case and c_{11}^{eff} change very slowly with the increasing modulus of the fluid filling the cracks, due to their less sensitivities to Z_{N}. It makes the horizontal P-wave velocity of the horizontal cracks case and the vertical P-wave velocity of the vertical cracks case increase very little, as shown in Fig. 11a and b. Therefore, we can conclude that degrees of the P- and SV-wave velocities anisotropy depend on the modulus of fluid filling the cracks. Conversely, the degree of the SH-wave velocity anisotropy is unrelated to the fluid modulus. For the case with tilted cracks, fluid saturation can also increase the elements related to the compressional moduli and has no effects on c_{55}^{eff} and c_{66}^{eff}. Nevertheless, F_{44} can be proven to be nonzero (exactly speaking, be negative) by substituting Eq. (20) into Eq. (24). As a result, the filling fluid will weaken the effect of the aligned cracks on c_{44}^{eff} and make the value of c_{44}^{eff} larger, as shown by the cyan solid lines in Fig. 10c and d.

3.3. Effect of crack density

The analyses in the previous subsection confirm that the velocities of the overall rock have higher sensitivities to the dry crack than the saturated crack. Moreover, maximums and minimums can be utilized to describe the characteristics of a function. Thus, this subsection mainly investigates variations of maximum and minimum velocities with the crack density for two cases of the vertical and horizontal dry cracks. The maximum and minimum velocities refer to the vertical and horizontal velocities for the P and SH waves and the SV-wave velocities at the 0° and around 45° incident angles.

Fig. 12 illustrates variations of the vertical and horizontal velocities with the crack density. Fig. 12a and b manifests that the P-wave velocities decrease approximately linearly with the crack density whether the aligned cracks are horizontal or vertical. However, the sensitivities (namely the slopes of the lines) of the P-wave velocities parallel to the crack plane to the crack density are extremely weak and far smaller than those of the P-wave velocities normal to the crack plane. These observations agree with some published experiment results (Ding et al., 2017; Shuai et al., 2020; Silva et al., 2019). Fig. 12a and b also reveals that the change of the background medium has little influence on the sensitivity of the P-wave velocity to the crack density. Likewise, the increase of the crack density slightly changes the sensitivities of the P-wave velocity to the background parameters for the case with the crack density less than 0.05. This is due to the fact that the P-wave velocity depends on the effective stiffness coefficients, and dominating contributions of the background medium and the cracks to the effective stiffness coefficients are nearly independent of each

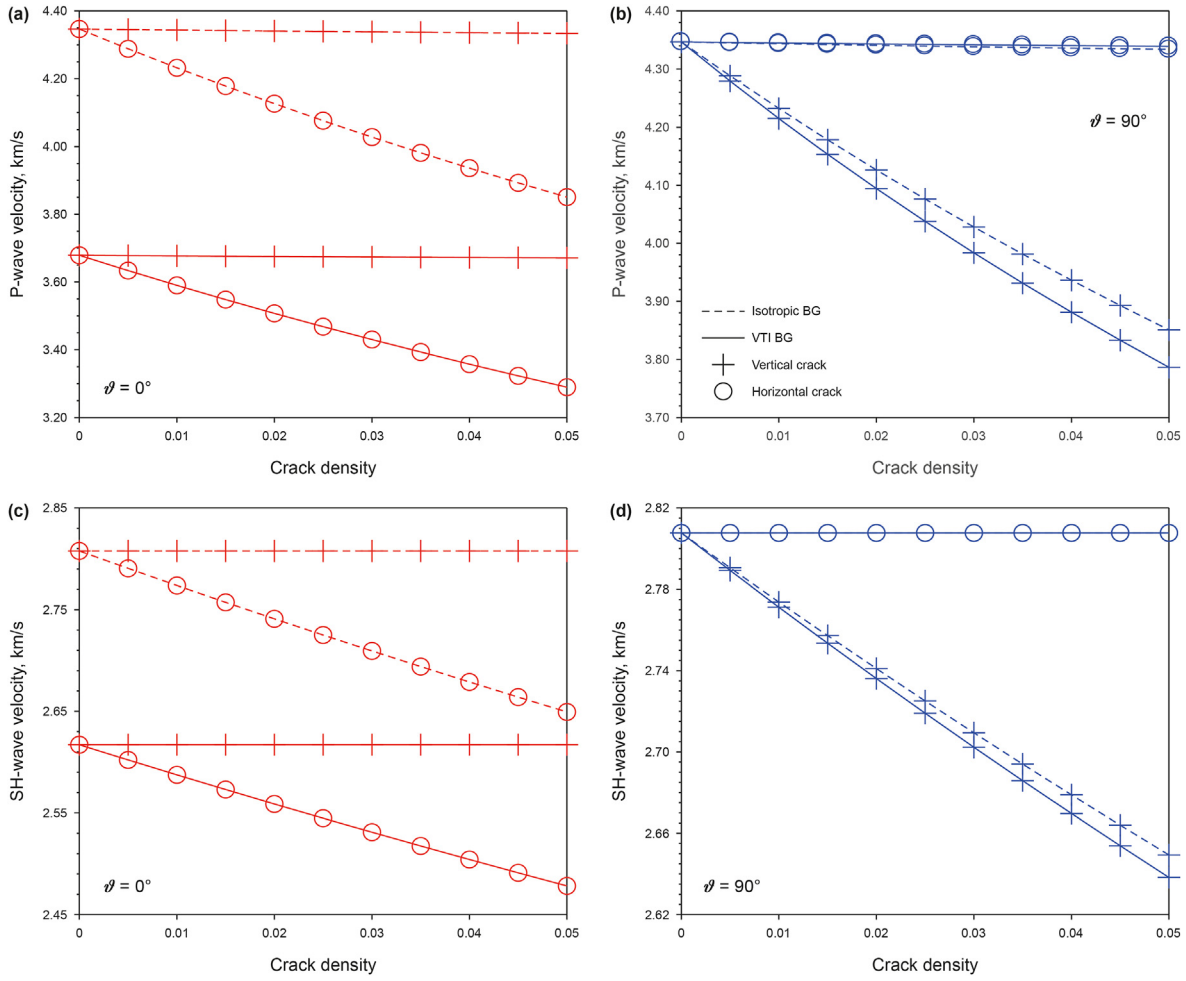

Fig. 12. Vertical (red lines) and horizontal (blue lines) velocities versus the crack density: (a and b) The P-wave velocities, (c and d) the SH-wave velocities. 'BG' represents 'background medium'.

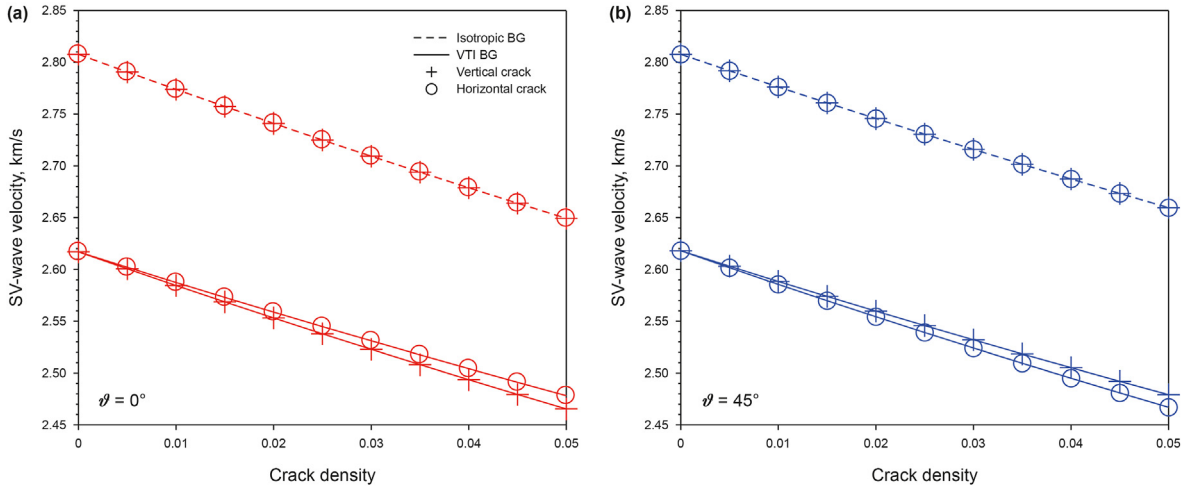

Fig. 13. SV-wave velocities at the (a) normal and (b) 45° incident angles versus the crack density. The meaning of the legend is identical with that in Fig. 12.

other as clarified by Eqs. (28) and (39). Furthermore, Fig. 11a and b demonstrates that the effects of the fluid on the P-wave velocities parallel to the crack plane are very small. Therefore, we can first give rough estimations about cracks parameters and fluid modulus, and then use the P-wave velocity parallel to the crack plane to predict the background parameters. Sil (2013) has used the vertical velocities from well logs to predict the parameters of the isotropic background.

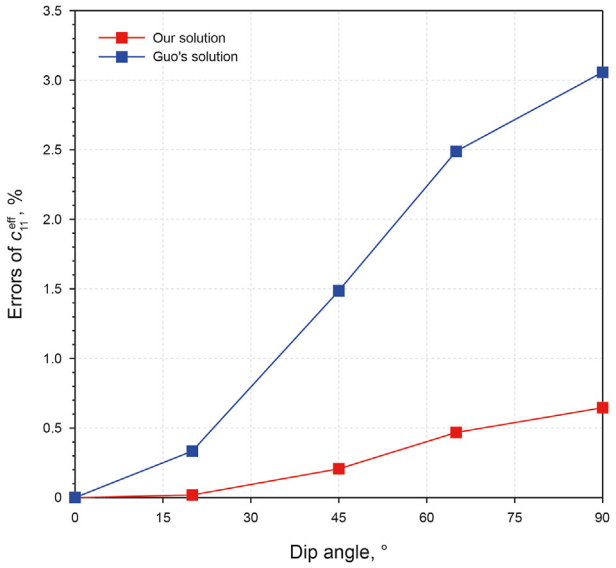

Fig. 14. Errors of the predicted c_{11}^{eff} versus the crack dip angle. The red and blue lines correspond to the approximate solutions given in this paper and by Guo et al. (2019), respectively.

Based on Fig. 12c and d, it can be concluded that the SH-wave velocity normal to the crack plane decreases linearly with the crack density. Nevertheless, the SH-wave velocity parallel to the crack plane is independent of the crack density, which results from the facts that the c_{55}^{eff} of the vertical crack case and c_{66}^{eff} of the horizontal crack case are unrelated to the crack density according to Eqs. (29) and (40). These conclusions are consistent with the experiment results given by Ding et al. (2017) and Silva et al. (2019). Similar to the P-wave velocity, the change of the background parameter has little effect on the sensitivity of the SH-wave velocity to the crack density. The increase of the crack density hardly changes the sensitivities of the SH-wave velocity to the background parameters. Besides, the filling fluid has no influence on the SH-wave velocity. Therefore, the SH-wave velocity parallel to the crack plane is another better choice to predict the background parameters. Fig. 13 illustrates that the SV-wave velocity is also a linearly decreasing function of the crack density. The background anisotropy and the incident angle have little effects on the sensitivity of the SV-wave velocity to the density of the dry crack. By comparing the dashed lines in Fig. 13, we infer that the SV-wave velocity depends very weakly on the dip angle of the dry crack in the isotropic background. Accordingly, the SV-wave velocity has potential applications in estimating the density of randomly oriented dry cracks in the isotropic background.

4. Discussion

4.1. Numerical verification of approximate solution accuracy

The conclusions in the above section are draw based on the proposed approximate solution illuminated by Eqs. (20)–(22). Although many conclusions have been justified by comparisons with other published studies, the accuracy of the proposed approximate solution still needs further verification. For the case with $\Delta_{\text{COD}}^{\text{H}} < 0$, the proposed approximate solution is equivalent to that given by Guo et al. (2019), which has been proved to be of high accuracy by a numerical experiment. For the case with $\Delta_{\text{COD}}^{\text{H}} > 0$, the stiffness parameters of the 26th sample (possessing big $\Delta_{\text{COD}}^{\text{H}}$, as shown in Fig. 8) in Table A-1 are utilized to assess the accuracy of the approximate solution by comparing with accurate results. The aspect ratio and density of the aligned cracks are set to 0.001 and 0.05, respectively. The accurate result can be obtained by the method given in the "Theoretical background". Fig. 14 shows variations of the errors of the approximate c_{11}^{eff} with the crack dip angle. The error is measured by substituting c_{ij}^{eff} for B_{ij} in Eq. (17). From Fig. 14, we can find that the errors of the predicted c_{11}^{eff} gradually increase with the crack dip angle and reach the maximums at the dip angle of 90°. For the horizontal crack case, both estimations based on our and Guo's approximate solutions are consistent with the accurate result. Nevertheless, the accuracy of our approximate solution is higher than that of Guo's for the non-horizontal crack case. Additionally, we calculate the errors of estimations of nine stiffness coefficients obtained by our and Guo's approximate solutions for the vertical crack case, as show in Fig. 15. We can see that the maximum error in Guo's estimations exceeds 9%, while the maximum error in our predictions is around equal to 2%. Therefore, the accuracy of our approximate solution is higher than that of Guo's approximate solution for the case with $\Delta_{\text{COD}}^{\text{H}} > 0$. In a conclusion, the proposed analytical solution for the effective elastic properties of the rock with the inclined circle cracks in the VTI background possesses the satisfactory accuracy.

4.2. Comparison with experimental data

To further demonstrate rationality and accuracy of the proposed approximate solution, we compare theoretical predictions of our solution with the ultrasonic measurements on a synthetic cracked sample by Silva et al. (2019). The synthetic sample is formed by vertical squared cracks in a layered background. Firstly, a mixture of fine sand, cement and water was poured into an acrylic model until the formation of a layer. This procedure was repeated to manufacture the VTI background. Furthermore, squared styrofoam cuts with an area of 4 cm^2 and a width of 0.08 cm were placed perpendicular to the first layer of deposition. After the sample was

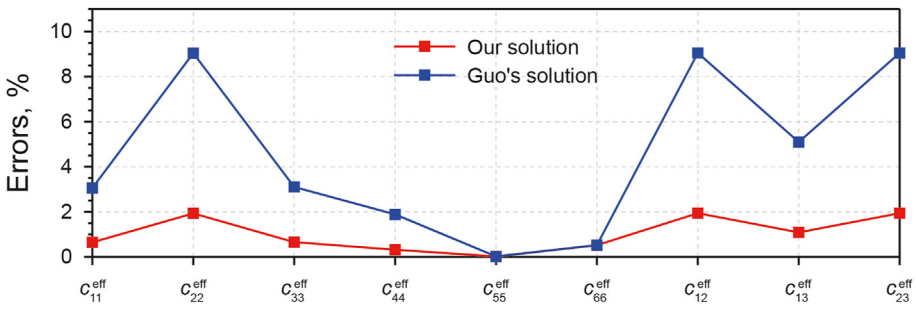

Fig. 15. Errors of predicted nine effective stiffness parameters for the vertical crack case.

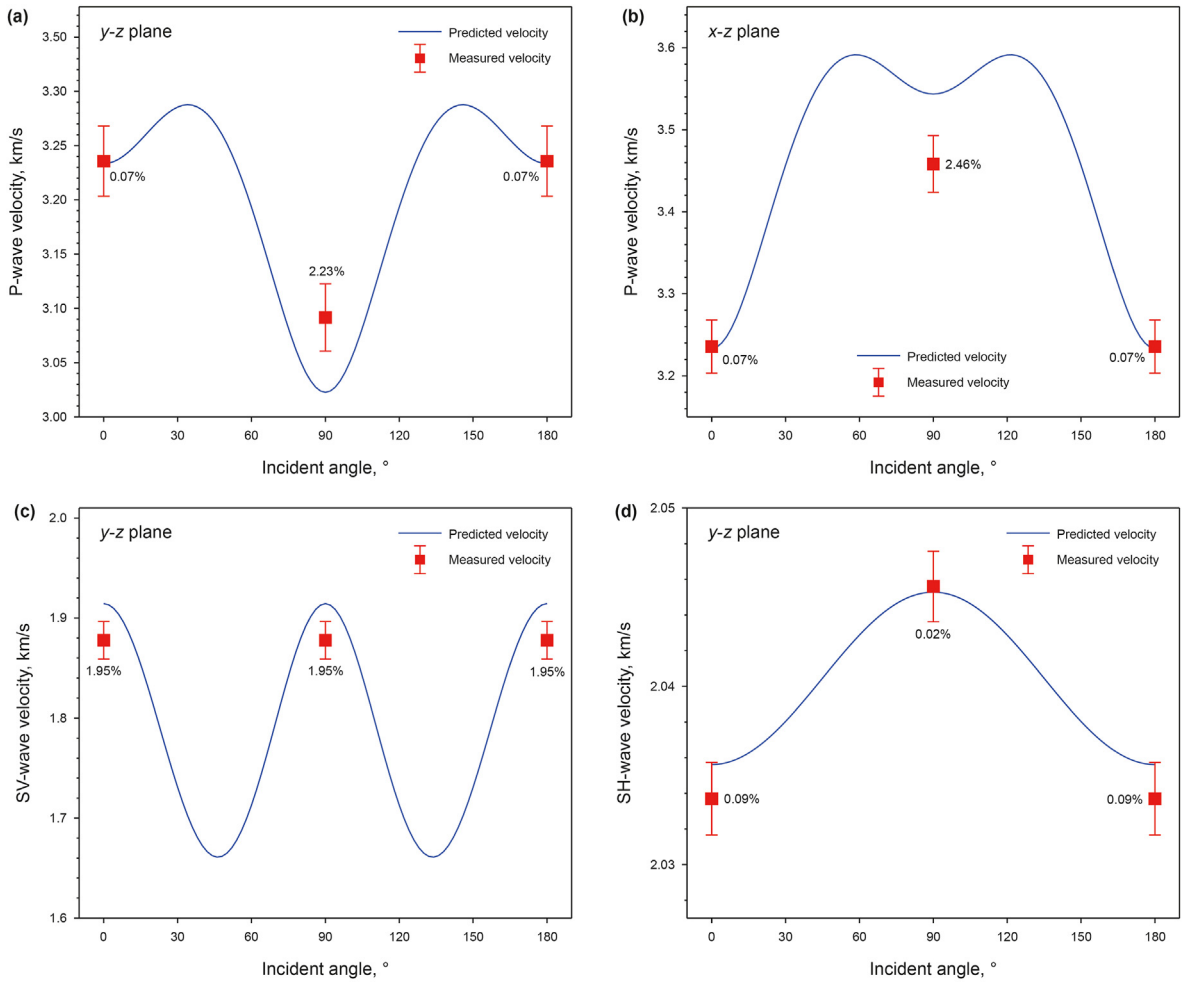

Fig. 16. Comparisons of predicted velocities (blue lines) of the (a) P, (c) SV and (d) SH waves in the *y*-*z* plane and (b) P wave in the *x*-*z* plane with measured velocities (red rectangles) of an orthorhombic sample (Silva et al., 2019).

dry, it was sprayed with water twice a day for eight days and then placed into an oven for about 2 h to make it rigid. Finally, the complete styrofoam cuts were dissolved by paint thinner to generate empty aligned squared cracks and the dry orthorhombic sample was complete. A reference sample (without cracks) with a volume of 128.795 cm^3 is utilized to obtain the property of the VTI background from the ultrasonic measurement. The mass density (ρ_0) and porosity of the reference sample are 1.911 g/cm^3 and 15.27%, respectively. In the *y* direction, the P-wave (V_{py}) velocity is 3626.7 m/s and the shear velocity of the wave polarized in the *x* axis (V_{sxy}) is 2227.3 m/s. In the *z* direction, the P-wave (V_{pz}) velocity is 3402 m/s and the shear velocity of the wave polarized in the *x* axis (V_{szx}) is 2065.4 m/s. Therefore, stiffness coefficients of the reference sample can be calculated by (Mavko et al., 2009)

$$c_{11}^0 = c_{22}^0 = \rho_0 V_{py}^2, c_{33}^0 = \rho_0 V_{pz}^2, c_{44}^0 = c_{55}^0 = \rho_0 V_{szx}^2, c_{66}^0 = \rho_0 V_{sxy}^2 \text{ and } c_{12}^0 = c_{11}^0 - 2c_{66}^0. \tag{48}$$

Since the P- and S-wave velocities at the 45° incident angle were not measured, we cannot obtain c_{13}^0 of the reference sample. According to the procedure of making the synthetic sample, we choose a relationship between c_{13}^0 and other stiffness coefficients to estimate c_{13}^0, which is given by (Yan et al., 2019)

$$c_{13}^0 = \sqrt{c_{33}^0 (c_{11}^0 - 2c_{66}^0)}. \tag{49}$$

Experimental data on the synthetic sample with three parallel vertical cracks are employed to compare with predictions of the proposed approximate solution. The mass density and porosity of the synthetic cracked sample are 1.821 g/cm^3 and 16.44%, respectively. Its volume (V_c) is 138.145 cm^3. The proposed approximate solution requires that the crack is penny-shaped. Thus, we equate the squared crack in this experiment with the penny-shaped crack, then the effective crack density of the penny-shaped cracks can be calculated by $e = N_c(S/\pi)^{1.5}/V_c$, where N_c is the number of the cracks and *S* represents the average area of the cracks plane. Because the background porosity of the cracked sample is different from that of the reference sample, the stiffness parameters of the reference sample cannot be directly regarded as those of the VTI background of the cracked sample even if their mineral compositions are the same. We combine the Backus average theory (Backus, 1962) with the critical porosity model to convert the stiffness parameters of the reference sample into those of the VTI background of the cracked sample. The conversion formulas are derived in Appendix C.

After obtaining the effective crack density and the stiffness parameters of the VTI background of the synthetic cracked sample, its effective stiffness parameters can be predicted using Eqs.

(36)–(43). Then the phase velocities can be estimated using Eqs. (B-1)–(B-6), which are displayed in Fig. 16. The errors of the predicted results can be assessed by substituting the velocities for B_{ij} in Eq. (17). From Fig. 16, we can find that the predicted results are in good agreement with the experimental data and the maximum error is less than 3%, which proves our solution reasonable again. Nevertheless, it should be noted that the crack is actually square in this orthorhombic sample, which does not satisfy the assumption of the proposed approximate solution. And c_{13}^0 of the synthetic reference sample was not measured. In the future, the experiment data on the orthorhombic sample with the vertical penny-shaped cracks are required to further verify our solution. Besides, the aligned cracks of the current synthetic samples are either parallel or perpendicular to the isotropic plane of the VTI background. To the best of our knowledge, no experimental data have been measured for a synthetic sample with aligned cracks inclined to the isotropic plane of the VTI background. Thus, we will try to manufacture such synthetic sample to further validate our model.

4.3. Stiffness contribution matrix of non-inclined cracks in weakly anisotropic background

The VTI rocks with weak anisotropy are rather common in the subsurface (Thomsen, 1986). When the VTI background is weakly anisotropic, $|\varepsilon|$, $|\gamma|$ and $|\delta|$ «1 and then we can neglect terms containing ε^2, δ^2, $\varepsilon\gamma$, $\varepsilon\delta$ and $\gamma\delta$ in Eq. (7). Thus, $G \approx c_{33}^0\sqrt{4g}\left(1+\frac{1+g}{4g}\varepsilon+\frac{g-1}{4g}\delta\right)$, $\xi \approx 1-2g+\delta$ so that Eqs. (5) and (6) can be simplified as

$$B_{11}^{\mathrm{hor}} = B_{22}^{\mathrm{hor}} \approx \frac{16a}{3\pi c_{33}^0 g(3-2g)}\left(1+\frac{g^2+1}{2g(2g-3)}\varepsilon+\frac{1}{2g-3}\gamma+\frac{g^2+2g-1}{2g(2g-3)}\delta\right), \tag{50}$$

$$B_{33}^{\mathrm{hor}} \approx \frac{4a}{3\pi c_{33}^0 g(1-g)}\left(1+\frac{5g^2-4g+1}{4g(g-1)}\varepsilon+\frac{g^2+2g-1}{4g(g-1)}\delta\right). \tag{51}$$

Owing to the hypothesis of the small crack density, the terms containing εe, γe and δe can also be omitted. For the dry horizontal crack case, by substituting Eqs. (50) and (51) into Eqs. (26) and (27), the crack compliance parameters can be approximated as

$$Z_N^{\mathrm{hor}} = \frac{\pi e}{a}B_{33}^{\mathrm{hor}} \approx \frac{4e}{3c_{33}^0 g(1-g)}, Z_{\mathrm{T}}^{\mathrm{hor}} = \frac{\pi e}{a}B_{11}^{\mathrm{hor}} \approx \frac{16e}{3c_{33}^0 g(3-2g)}. \tag{52}$$

Further, the crack weakness parameters can be written as linear functions of the crack density, namely

$$\Delta_{\mathrm{N}}^{\mathrm{hor}} \approx c_{33}^0 Z_{\mathrm{N}}^{\mathrm{hor}} = \frac{4e}{3g(1-g)}, \Delta_{\mathrm{T}}^{\mathrm{hor}} \approx c_{44}^0 Z_{\mathrm{T}}^{\mathrm{hor}} = \frac{16e}{3(3-2g)}. \tag{53}$$

According to the definitions of the Thomsen's parameters, we can obtain

$$c_{11}^0 = (1+2\varepsilon)c_{33}^0, c_{66}^0 = (1+2\gamma)gc_{33}^0$$

$$c_{13}^0 = \left\{-g+(1-g)[1+2\delta/(1-g)]^{1/2}\right\}c_{33}^0 \approx (1-2g+\delta)c_{33}^0 \tag{54}$$

Substituting Eqs. (53) and (54) into Eq. (29) and neglecting the second-order terms of the Thomsen's parameters and the crack density, the stiffness contribution matrix of the dry horizontal cracks in weakly anisotropic background can be derived as

$$\mathbf{C}_{\mathrm{c}}^{\mathrm{hor}} = -c_{33}^0\begin{bmatrix} (1-2g)^2\Delta_{\mathrm{N}}^{\mathrm{hor}} & (1-2g)^2\Delta_{\mathrm{N}}^{\mathrm{hor}} & (1-2g)\Delta_{\mathrm{N}}^{\mathrm{hor}} & 0 & 0 & 0 \\ (1-2g)^2\Delta_{\mathrm{N}}^{\mathrm{hor}} & (1-2g)^2\Delta_{\mathrm{N}}^{\mathrm{hor}} & (1-2g)\Delta_{\mathrm{N}}^{\mathrm{hor}} & 0 & 0 & 0 \\ (1-2g)\Delta_{\mathrm{N}}^{\mathrm{hor}} & (1-2g)\Delta_{\mathrm{N}}^{\mathrm{hor}} & \Delta_{\mathrm{N}}^{\mathrm{hor}} & 0 & 0 & 0 \\ 0 & 0 & 0 & g\Delta_{\mathrm{T}}^{\mathrm{hor}} & 0 & 0 \\ 0 & 0 & 0 & 0 & g\Delta_{\mathrm{T}}^{\mathrm{hor}} & 0 \\ 0 & 0 & 0 & 0 & 0 & 0 \end{bmatrix} \tag{55}$$

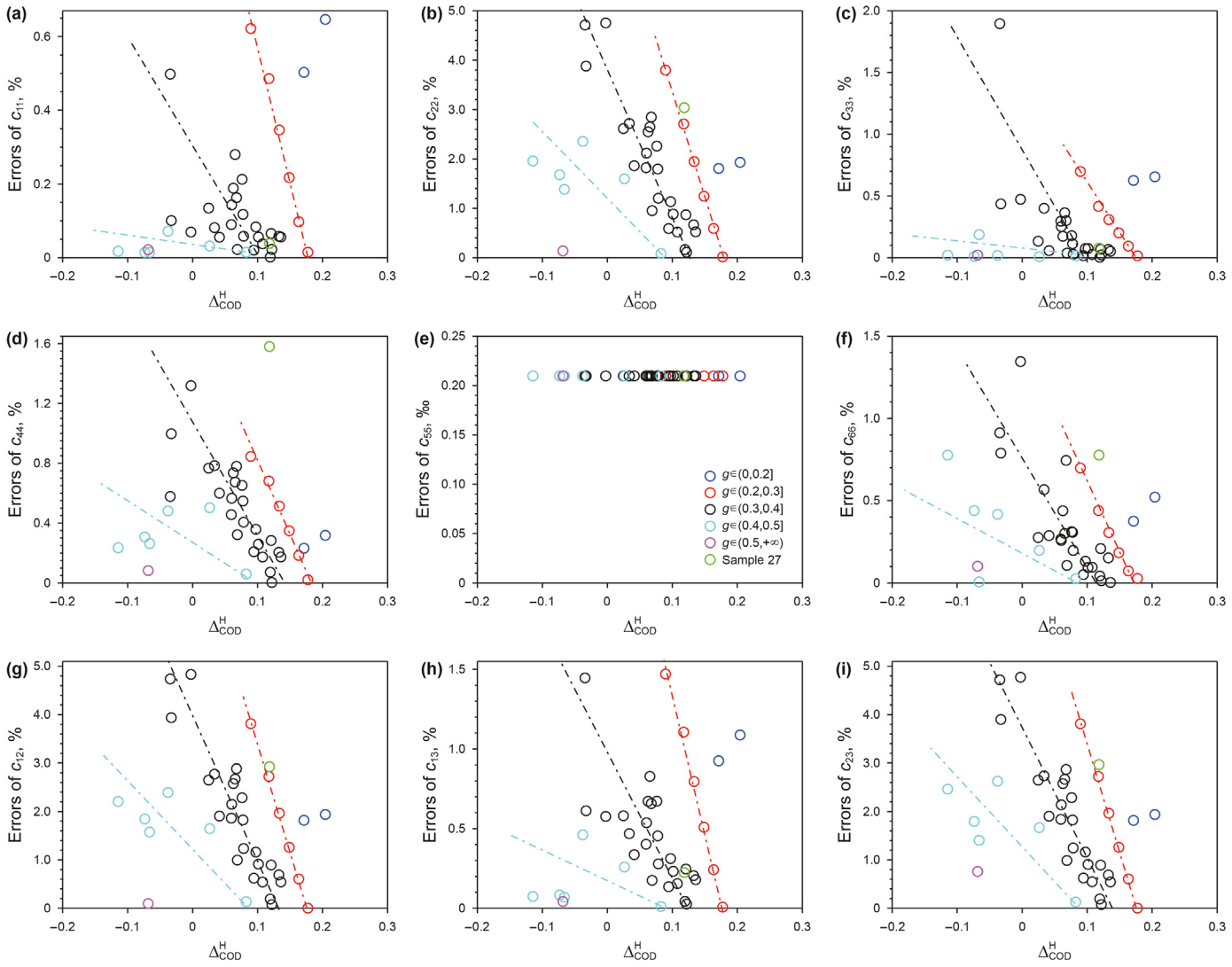

Fig. 17. Variations of errors of approximate stiffness parameters with Δ^{H}_{COD}. (a) c_{11}, (b) c_{22}, (c) c_{33}, (d) c_{44}, (e) c_{55}, (f) c_{66}, (g) c_{12}, (h) c_{13}, and (i) c_{23}.

If the background medium is further assumed to be isotropic, stiffness contribution Eq. (55) will be consistent with the first-order term of the Hudson model (Hudson, 1980, Eq. (51)).

It can be inferred from Fig. 2 that when the VTI background possesses weak anisotropy, $\Delta^{H}_{COD}>0$ so that $\lambda_n=1$ in Eqs. (36)–(38). Therefore, for the case of the dry vertical cracks, analogous to derivations in the dry horizontal crack case, Eq. (40) can be simplified to

$$\mathbf{C}_c^{ver} \approx -c_{33}^0 \begin{bmatrix} (1-2g)^2\Delta_N^{ver} & (1-2g)\Delta_N^{ver} & (1-2g)^2\Delta_N^{ver} & 0 & 0 & 0 \\ (1-2g)\Delta_N^{ver} & \Delta_N^{ver} & (1-2g)\Delta_N^{ver} & 0 & 0 & 0 \\ (1-2g)^2\Delta_N^{ver} & (1-2g)\Delta_N^{ver} & (1-2g)^2\Delta_N^{ver} & 0 & 0 & 0 \\ 0 & 0 & 0 & g\Delta_V^{ver} & 0 & 0 \\ 0 & 0 & 0 & 0 & 0 & 0 \\ 0 & 0 & 0 & 0 & 0 & g\Delta_H^{ver} \end{bmatrix} \tag{56}$$

where

$$\Delta_N^{ver} \approx \frac{4e}{3g(1-g)}, \Delta_V^{ver} \approx \Delta_H^{ver} \approx \frac{16e}{3(3-2g)} \quad (57)$$

Hudson (1991) pointed out that weakly anisotropic material could be modeled as an isotropic matrix containing aligned cracks. We utilize an isotropic matrix with horizontal cracks to model the VTI background and the compressional and shear moduli of the isotropic matrix are c_{33}^0 and c_{44}^0, respectively. Thus, stiffness contribution Eq. (56) will be identical with the first-order perturbation of the stiffness contribution matrix of the vertical cracks in the weakly anisotropic VTI background given by Hudson (1991, Eq. (31)). The above analyses prove once again that the model proposed in this paper is reasonable.

It can be found from Eqs. (55) and (56) that the stiffness contribution matrixes of the non-inclined cracks only depend on the crack density, c_{33}^0 and g for the case of the weakly anisotropic background. Therefore, it is possible to utilize only vertical P- and S-wave velocities from seismic or other data for predicting the crack density in the field with approximately constant g. This is not the focus of this paper. More detailed studies will be implemented in the future.

4.4. Effect of background anisotropy degree on the accuracy of the approximate solution

According to the investigation in the above subsection, the error of the approximate solution is largest for the vertical crack case. Consequently, we will only discuss the effect of the background anisotropy degree on the accuracy of the approximate solution of the vertical crack case. It can be inferred from Fig. 2 that when g is constant, $(B_{22}^{hor} - B_{33}^{hor})$ will decrease with the increase of the degree of the background anisotropy, so that Δ_{COD}^H will decrease from positive to negative. Therefore, Δ_{COD}^H can be utilized as an overall measure of the degree of the background anisotropy, that is, the smaller value of Δ_{COD}^H reflects the higher degree of the background anisotropy.

Forty groups of stiffness coefficients of the VTI media employed in Fig. 8 are utilized to calculate the effective stiffness coefficients of dry rocks with the VTI background permeated by the vertical cracks. The aspect ratio and density of the crack are 0.001 and 0.05, respectively. The exact effective stiffness coefficients can be obtained by combining Eqs. (1) and (3). The approximate stiffness coefficients are calculated using Eqs. (39)–(43). The error of the approximate value is measured by substituting c_{ij} for B_{ij} in Eq. (17). Fig. 17 shows variations of the errors with Δ_{COD}^H. The green circle in Fig. 17 corresponds to the 27th sample. Because the property of the 27th sample is very scarce in the subsurface, the green data point will be ignored in the following discussion. The circles in other colors correspond to the cases with different values of g, respectively, as illustrated by the legend in Fig. 17e. From Fig. 17a–d and 17f-i, it can be seen that the errors of c_{11}, c_{22}, c_{33}, c_{44}, c_{66}, c_{12}, c_{13} and c_{23} decrease approximately linearly with the increase of Δ_{COD}^H. From Fig. 17e, we find that the error of c_{55} is almost independent of the value of Δ_{COD}^H. This is due to the fact that the errors in predicting stiffness parameters are mainly generated by the approximations of the crack weakness parameters and the numerical rounding of the calculation process. According to Eqs. (39) and (40), c_{55} of the vertical crack case is unrelated to the crack weakness parameters. Hence, the errors exhibited in Fig. 17e come only from the numerical rounding of the calculation process and are independent of the value of Δ_{COD}^H. Likewise, c_{11} is less dependent on the crack weakness parameters according to Eq. (40), so that its total error is very small as shown in Fig. 17a. Consequently, the random error caused by the numerical rounding accounts for a relatively high proportion of the total error, which results in the black circles in Fig. 17a being more dispersed than those in other Figures. Based on the above discussions, we conclude that the higher degree of the background anisotropy may lead to the lower accuracy of the approximate solution without consideration of the numerical rounding.

5. Conclusions

In this work, we studied the effective elastic properties of the rock with the inclined penny-shaped cracks in the transversely isotropic background. By forty groups of numerical experiments, we have confirmed that when $\Delta_{COD}^H > 0$, the CODs are less dependent on the crack dip angle in the coordinate formed by the crack plane. Conversely, the CODs are less dependent on the crack dip angle in the coordinate formed by the symmetry axes of the VTI background. From this conclusion, the COD tensor of the circle crack in the isotropic plane of the VTI background was then approximately extended to the case with cracks inclined to the isotropic plane. Using the relationship between the COD tensor and the crack compliance contribution tensor, we further derived the analytical forms of the effective compliance matrixes of the dry and saturated rocks with the tilted cracks in the VTI background, respectively.

To analyze the effects of the crack dip angle, background anisotropy, filling fluid and crack density on the effective elastic properties of the cracked rock, we investigated two tight sand cracked samples with the VTI and isotropic backgrounds, respectively. The growing crack dip angle may make the anisotropy of the P- and SH-wave velocities reduce to zero first, and then increase inversely, but the specific effects are related to the crack density and the degree of the background anisotropy. The background anisotropy also has noteworthy influences on the anisotropy of the P- and SH-wave velocities, and the influences are dependent on the crack density and the dip angle. Unlike the P- and SH-wave velocities, the crack dip angle and the background anisotropy have relatively small effects on the change of the SV-wave velocity with the incident angle. For the non-inclined cracks case, filling fluid only raises the stiffness coefficients related to the compressional modulus. However, for the inclined cracks case, filling fluid also changes the stiffness coefficients related to the shear modulus besides those related to the compressional modulus. Additionally, the background anisotropy slightly modifies decreasing rates of the velocities with the crack density. The crack dip angle has great influences on the decreasing rates of the P- and SH-wave velocities with the crack density, while its effect on the decreasing rate of the SV-wave velocity needs further researches in the future. For the vertical crack case with the weak background anisotropy, the proposed model is consistent with Hudson's published first-order correction theory for the orthorhombic rock developed by two orthogonal sets of aligned cracks. The exact numerical results and experimental data demonstrated that the proposed model could realize predictions of effective stiffness coefficients with high accuracies. Nevertheless, it may be difficult to acquire the relatively accurate estimation with this model for the case with extremely strong background anisotropy. Meantime, the proposed model requires the crack to be penny-shaped and its concentration to be dilute.

Declaration of competing interest

The authors declare that they have no known competing

financial interests or personal relationships that could have appeared to influence the work reported in this paper.

Acknowledgements

We would like to acknowledge all the reviewers and editors and the sponsorship of National Natural Science Foundation of China (42030103), the Marine S&T Fund of Shandong Province for Pilot National Laboratory for Marine Science and Technology (Qingdao) (2021QNLM020001-6), the Laoshan National Laboratory of Science and Technology Foundation (LSKJ202203400).

Appendix A. The 35 groups of measured data of VTI rocks

We collect the 35 groups of the stiffness coefficients of rock samples from a variety of the VTI strata, as in Table A-1.

Table A-1
Measured stiffness coefficients and densities of 35 rock samples.

No.	Rock samples, depth, ft	C_{11}, GPa	C_{33}, GPa	C_{44}, GPa	C_{66}, GPa	C_{13}, GPa	ρ, g × cm^{-3}
1	Mesaverde mudshale (4903)[1]	55.204	51.689	18.411	20.105	24.405	2.520
2	Mesaverde immature sandstone (4912)[1]	59.803	50.086	19.796	21.815	14.751	2.500
3	Mesaverde immature sandstone (4946)[1]	47.503	41.164	13.484	15.264	14.604	2.450
4	Mesaverde silty limestone (5469.5)[1]	72.297	65.015	22.103	25.064	20.614	2.630
5	Mesaverde immature sandstone (5555.5)[1]	57.225	51.094	18.159	19.794	21.412	2.480
6	Mesaverde laminated siltstone (5566.3)[1]	60.127	50.869	17.173	18.753	38.255	2.570
7	Mesaverde immature sandstone (5837.5)[1]	56.394	53.914	19.823	20.339	14.373	2.470
8	Mesaverde immature sandstone (6455.1)[1]	52.889	47.820	16.396	20.758	21.843	2.450
9	Mesaverde immature sandstone (6542.6)[1]	56.496	48.704	16.219	19.235	16.119	2.510
10	Mesaverde mudshale (6563.7)[1]	70.350	68.970	24.087	23.846	21.615	2.680
11	Mesaverde sandstone (7888.4)[1]	63.179	59.267	21.184	20.379	19.199	2.500
12	Mesaverde mudshale (7939.5)[1]	57.045	49.092	16.242	17.801	22.427	2.660
13	Mesaverde shale (350)[2]	30.391	26.895	13.968	15.951	0.458	2.350
14	Mesaverde shale (1599)[2]	51.182	40.174	18.989	19.977	1.707	2.640
15	Mesaverde shale (1968)[2]	71.130	63.171	27.031	28.545	9.609	2.690
16	Mesaverde shale (3511)[2]	71.759	53.392	26.105	34.302	1.181	2.810
17	Mesaverde shale (3883)[2]	51.546	41.040	20.059	24.071	3.910	2.920
18	CottonValley shale[3]	74.727	58.840	22.049	29.987	25.290	2.640
19	Pierre shale[4]	11.237	10.910	2.113	2.239	7.316	2.250
20	Green River shale1[5]	43.319	40.111	13.663	14.483	13.183	2.310
21	Green River shale2[5]	47.043	44.803	15.400	16.016	16.371	2.310
22	Berea sandstone[6]	38.009	37.858	15.187	15.339	8.228	2.140
23	Bandera sandstone[6]	33.236	31.355	12.112	12.839	8.493	2.160
24	Lance sandstone[7]	60.842	61.457	21.681	21.898	17.162	2.430
25	Ft. Union siltstone[7]	67.407	61.841	22.489	24.288	13.975	2.600
26	Timber Mtn tuff[7]	56.906	54.717	8.026	9.712	36.993	2.330
27	Quartz crystal[8]	79.570	98.477	53.210	36.289	13.745	2.650
28	Apatite crystal[8]	154.44	129.349	61.989	71.784	59.456	3.218
29	“Sandstone-shale"[9]	21.737	21.187	6.402	6.850	8.362	2.340
30	“SS-anisotropic shale"[9]	23.687	21.187	6.402	8.488	8.362	2.340
31	“Anisotropic shale"[9]	21.264	17.632	5.321	8.993	6.972	2.340
32	“Gas sand-water sand"[9]	4.207	4.030	1.235	1.245	1.632	2.030
33	Brine-saturated Africa shales (7815.0)[10]	32.22	27.2	6.85	8.66	14.45	2.408
34	Brine-saturated tight sands (11868.4)[10]	73.27	70.41	21.91	24.1	24.95	2.639
35	Gas-saturated tight sands (11868.4)[10]	60.93	54.15	21.05	23.7	12.87	2.598

[1]Thomsen (1986), [2]Lin (1984), [3]Tosaya (1982), [4]White et al. (1983), [5]Podio et al. (1968), [6]King (1964), [7]Schock et al. (1974), [8]Simmons and Wang (1971), [9]Levin (1979), [10]Wang (2002).

Appendix B. Phase velocity of the orthorhombic linear elastic rock

For the orthorhombic linear elastic medium, the phase velocities of seismic waves in the different coordinate planes can be calculated using the effective stiffness parameters (Mavko et al., 2009). The phase velocities of the waves propagating in the *y*-*z* plane can be expressed as follows:

$$V_{\mathrm{P}}=\left(c_{44}+c_{22}\sin^2\vartheta+c_{33}\cos^2\vartheta+\sqrt{\left(c_{44}+c_{22}\sin^2\vartheta+c_{33}\cos^2\vartheta\right)^2-4\Gamma}\right)^{1/2}(2\rho)^{-1/2}, \tag{B-1}$$

$$V_{\mathrm{SV}}=\left(c_{44}+c_{22}\sin^2\vartheta+c_{33}\cos^2\vartheta-\sqrt{\left(c_{44}+c_{22}\sin^2\vartheta+c_{33}\cos^2\vartheta\right)^2-4\Gamma}\right)^{1/2}(2\rho)^{-1/2}, \tag{B-2}$$

$$V_{\mathrm{SH}}=\left(\frac{c_{66}\sin^2\vartheta+c_{55}\cos^2\vartheta}{\rho}\right)^{1/2}, \tag{B-3}$$

where c_{ij} and ρ are the ij stiffness element and the mass density of the overall orthorhombic medium, respectively. ϑ represents the angle between the incident direction and the z-axis and the expression of Γ is

$$\Gamma=\left(c_{22}\sin^2\vartheta+c_{44}\cos^2\vartheta\right)\left(c_{44}\sin^2\vartheta+c_{33}\cos^2\vartheta\right)-(c_{23}+c_{44})^2\sin^2\vartheta\cos^2\vartheta. \tag{B-4}$$

The velocity of the P wave propagating in the x-z plane can be expressed as follows:

$$V_{\mathrm{P}}=\left(c_{55}+c_{11}\sin^2\beta+c_{33}\cos^2\beta+\sqrt{\left(c_{55}+c_{11}\sin^2\beta+c_{33}\cos^2\beta\right)^2-4\Psi}\right)^{1/2}(2\rho)^{-1/2}, \tag{B-5}$$

where β represents the angle between the incident direction and the z-axis and the expression of Ψ is

$$\Psi=\left(c_{11}\sin^2\beta+c_{55}\cos^2\beta\right)\left(c_{55}\sin^2\beta+c_{33}\cos^2\beta\right)-(c_{13}+c_{55})^2\sin^2\beta\cos^2\beta. \tag{B-6}$$

Appendix C. Stiffness parameters conversion from reference sample to VTI background of cracked sample

We can transform the stiffness parameters of the reference sample into those of the VTI background of the cracked sample by a transformation formula. Taking c_{11}^0 as an example, we give derivation of the transformation formula. The reference sample and the VTI background of the cracked sample both consist of many isotropic layers. Assume that the compressional and shear moduli of each layer are equal to M and μ, respectively, and the porosity of each layer is φ. According to the critical porosity model,

$$M=M_{\mathrm{m}}(1-\varphi/\varphi_{\mathrm{cr}})\ \text{and}\ \mu=\mu_{\mathrm{m}}(1-\varphi/\varphi_{\mathrm{cr}}), \tag{C-1}$$

where the subscript 'm' indicates the matrix of each layer. φ_{cr} denotes the critical porosity and is set to 0.31 in this paper. Based on the Backus average theory (Backus, 1962),

$$c_{11}^0=\langle M-M^{-1}(M-2\mu)^2\rangle+\langle M^{-1}\rangle^{-1}\langle(M-2\mu)M^{-1}\rangle^2, \tag{C-2}$$

where the operator $\langle\bullet\rangle$ indicates taking the average by volume. Assuming that the subscript 'a' and 'b' represent the reference sample and the VTI background of the cracked sample, respectively. $M_{\mathrm{ma}}=M_{\mathrm{mb}}$ and $\mu_{\mathrm{ma}}=\mu_{\mathrm{mb}}$. Therefore, $c_{11\mathrm{b}}^0$ of the VTI background of the cracked sample is

$$\begin{aligned}c_{11\mathrm{b}}^0&=\langle M_{\mathrm{b}}-M_{\mathrm{b}}^{-1}(M_{\mathrm{b}}-2\mu_{\mathrm{b}})^2\rangle+\langle M_{\mathrm{b}}^{-1}\rangle^{-1}\langle(M_{\mathrm{b}}-2\mu_{\mathrm{b}})M_{\mathrm{b}}^{-1}\rangle^2\\&=\frac{(1-\varphi_{\mathrm{b}}/\varphi_{\mathrm{cr}})}{(1-\varphi_{\mathrm{a}}/\varphi_{\mathrm{cr}})}\left[\langle M_{\mathrm{a}}-M_{\mathrm{a}}^{-1}(M_{\mathrm{a}}-2\mu_{\mathrm{a}})^2\rangle+\langle M_{\mathrm{a}}^{-1}\rangle^{-1}\langle(M_{\mathrm{a}}-2\mu_{\mathrm{a}})M_{\mathrm{a}}^{-1}\rangle^2\right]\\&=c_{11\mathrm{a}}^0(1-\varphi_{\mathrm{b}}/\varphi_{\mathrm{cr}})/(1-\varphi_{\mathrm{a}}/\varphi_{\mathrm{cr}}).\end{aligned} \tag{C-3}$$

Likewise, other stiffness parameters of the VTI background of the cracked sample can be expressed as

$$c^0_{ijb} = c^0_{ija}(1 - \varphi_b / \varphi_{cr}) / (1 - \varphi_a / \varphi_{cr}). \quad \text{(C-4)}$$

References

Backus, G.E., 1962. Long-wave elastic anisotropy produced by horizontal layering. J. Geophys. Res. 67, 4427–4440. https://doi.org/10.1029/JZ067i011p04427.

Brown, R.J.S., Korringa, J., 1975. On the dependence of the elastic properties of a porous rock on the compressibility of the pore fluid. Geophysics 40, 608–616. https://doi.org/10.1190/1.1440551.

Chen, H., Ji, Y., Innanen, K.A., 2018. Estimation of modified fluid factor and dry fracture weaknesses using azimuthal elastic impedance. Geophysics 83, A73–A88. https://doi.org/10.1190/geo2017-0075.1.

Chen, H., Zhang, G., 2017. Estimation of dry fracture weakness, porosity, and fluid modulus using observable seismic reflection data in a gas-bearing reservoir. Surv. Geophys. 38, 651–678. https://doi.org/10.1007/s10712-017-9410-x.

Cheng, C.H., 1993. Crack models for a transversely isotropic medium. J. Geophys. Res. Solid Earth 98, 675–684. https://doi.org/10.1029/92JB02118.

Cheng, J., Zhang, F., Li, X., 2022. Seismic amplitude inversion for orthorhombic media based on a modified reflection coefficient approximation. Surv. Geophys. 43 (5), 1395–1433. https://doi.org/10.1007/s10712-022-09718-z.

Ding, P., Di, B., Wang, D., et al., 2017. Measurements of seismic anisotropy in synthetic rocks with controlled crack geometry and different crack densities. Pure Appl. Geophys. 174 (5), 1907–1922. https://doi.org/10.1007/s00024-017-1520-3.

Eshelby, J.D., 1957. The determination of the elastic field of an ellipsoidal inclusion, and related problems. Proc. Royal Soc. A: Math. Phys. Engi. Sci. 241 (1226), 376–396. https://doi.org/10.1098/rspa.1957.0133.

Fabrikant, V.I., 1989. Applications of Potential Theory in Mechanics: a Selection of New Results. Kluwer Academic Publishers, Dordrecht.

Giraud, A., Huynh, Q.V., Hoxha, D., et al., 2007. Effective poroelastic properties of transversely isotropic rock-like composites with arbitrarily oriented ellipsoidal inclusions. Mech. Mater. 39 (11), 1006–1024. https://doi.org/10.1016/j.mechmat.2007.05.005.

Guerrero, F., Sevostianov, I., Giraud, A., 2007. On an arbitrarily oriented crack in a transversely-isotropic medium. Int. J. Fract. 148 (3), 273–279. https://doi.org/10.1007/s10704-008-9191-9.

Guo, J., Han, T., Fu, L.Y., et al., 2019. Effective elastic properties of rocks with transversely isotropic background permeated by aligned penny-shaped cracks. J. Geophys. Res. Solid Earth 124 (1), 400–424. https://doi.org/10.1029/2018JB016412.

Guo, J., Rubino, J.G., Glubokovskikh, S., et al., 2017. Effects of fracture intersections on seismic dispersion: theoretical predictions versus numerical simulations. Geophys. Prospect. 65 (5), 1264–1276. https://doi.org/10.1111/1365-2478.12474.

Guo, J., Zhao, L., Yang, Z., et al., 2021. Analytical model for rock effective elastic properties with aligned elliptical cracks embedded in transversely isotropic background. Geophys. Prospect. 69 (7), 1515–1530. https://doi.org/10.1111/1365-2478.13105.

Hoenig, A., 1978. The behavior of a flat elliptical crack in an anisotropic elastic body. Int. J. Solid Struct. 14 (11), 925–934. https://doi.org/10.1016/0020-7683(78)90068-9.

Huang, L., Stewart, R.R., Sil, S., et al., 2015. Fluid substitution effects on seismic anisotropy. J. Geophys. Res. Solid Earth 120 (2), 850–863. https://doi.org/10.1002/2014JB011246.

Hudson, J.A., 1980. Overall properties of a cracked solid. Math. Proc. Cambridge 88 (2), 371–384. https://doi.org/10.1017/S0305004100057674.

Hudson, J.A., 1988. Seismic wave propagation through material containing partially saturated cracks. Geophys. J. Int. 92 (1), 33–37. https://doi.org/10.1111/j.1365-246X.1988.tb01118.x.

Hudson, J.A., 1991. Crack distributions which account for a given seismic anisotropy. Geophys. J. Int. 104 (3), 517–521. https://doi.org/10.1111/j.1365-246X.1991.tb05698.x.

Hudson, J.A., Liu, E., Crampin, S., 1996. The mechanical properties of materials with interconnected cracks and pores. Geophys. J. Int. 124 (1), 105–112. https://doi.org/10.1111/j.1365-246X.1996.tb06355.x.

Jakobsen, M., Hudson, J.A., Johansen, T.A., 2003. T-matrix approach to shale acoustics. Geophys. J. Int. 154 (2), 533–558. https://doi.org/10.1046/j.1365-246X.2003.01977.x.

Kachanov, M., 1992. Effective elastic properties of cracked solids: critical review of some basic concepts. Appl. Mech. Rev. 45 (8), 304–335. https://doi.org/10.1115/1.3119761.

Kalra, S., Tian, W., Wu, X., 2018. A numerical simulation study of CO2 injection for enhancing hydrocarbon recovery and sequestration in liquid-rich shales. Petrol. Sci. 15 (1), 103–115. https://doi.org/10.1007/s12182-017-0199-5.

King, M.S., 1964. Wave Velocities and Dynamic Elastic Moduli of Sedimentary Rocks. Ph.D. thesis. University of California, Berkeley.

Kuster, G.T., Toksöz, M.N., 1974. Velocity and attenuation of seismic waves in two phase media: Part 1. Theoretical formulation. Geophysics 39 (5), 587–606. https://doi.org/10.1190/1.1440450.

Levin, F.K., 1979. Seismic velocities in transversely isotropic media. Geophysics 44 (5), 918–936. https://doi.org/10.1190/1.1440985.

Lin, W., 1984. Ultrasonic velocities and dynamic elastic moduli of mesaverde rocks. In: Lawrence Livermore Nat. Lab. Rep. Lawrence Livermore National Lab.

Liu, Y., Liu, X., Lu, Y., et al., 2018. Fracture prediction approach for oil-bearing reservoirs based on AVAZ attributes in an orthorhombic medium. Petrol. Sci. 15 (3), 510–520. https://doi.org/10.1007/s12182-018-0250-1.

Lu, C., Lu, Y., Guo, J., et al., 2020. Stability of the formation interface under the impact of hydraulic fracture propagation in the vicinity of the formation interface. Petrol. Sci. 17 (4), 1101–1118. https://doi.org/10.1007/s12182-019-00416-x.

Mavko, G., Mukerji, T., Dvorkin, J., 2009. The Rock Physics Handbook-Tools for Seismic Analysis of Porous Media. Cambridge University Press, New York. https://doi.org/10.1017/CBO9780511626753.

Norris, A.N., 1985. A differential scheme for the effective moduli of composites. Mech. Mater. 4 (1), 1–16. https://doi.org/10.1016/0167-6636(85)90002-X.

O'Connell, R.J., Budiansky, B., 1974. Seismic velocities in dry and saturated cracked solids. J. Geophys. Res. 79 (35), 5412–5426. https://doi.org/10.1029/JB079i035p05412.

Podio, A.L., Gregory, A.R., Gray, K.E., 1968. Dynamic properties of dry and water-saturated green river shale under stress. Soc. Petrol. Eng. J. 8, 389–404. https://doi.org/10.2118/1825-PA, 04.

Schock, R.N., Bonner, B.P., Louis, H., 1974. Collection of Ultrasonic Velocity Data as a Function of Pressure for Polycrystalline Solids. Lawrence Livermore Nat. Lab. Rep, Lawrence Livermore National Lab. https://doi.org/10.2172/4293131.

Schoenberg, M., Douma, J., 1988. Elastic wave propagation in media with parallel fractures and aligned cracks. Geophys. Prospect. 36 (6), 571–590. https://doi.org/10.1111/j.1365-2478.1988.tb02181.x.

Schoenberg, M., Helbig, K., 1997. Orthorhombic media: modeling elastic wave behavior in a vertically fractured earth. Geophysics 62 (6), 1954–1974. https://doi.org/10.1190/1.1444297.

Sevostianov, I., Yilmaz, N., Kushch, V., et al., 2005. Effective elastic properties of matrix composites with transversely-isotropic phases. Int. J. Solid Struct. 42 (2), 455–476. https://doi.org/10.1016/j.ijsolstr.2004.06.047.

Sevostianov, I., Kachanov, M., 1999. Compliance tensors of ellipsoidal inclusions. Int. J. Fract. 96 (1), 3–7. https://doi.org/10.1023/A:1018712913071.

Seyedkavoosi, S., Vilchevskaya, E., Sevostianov, I., 2018. Randomly oriented cracks in a transversely isotropic material. Int. J. Solid Struct. 150, 222–229. https://doi.org/10.1016/j.ijsolstr.2018.06.013.

Shuai, D., Wei, J., Di, B., et al., 2020. Experimental study of crack density influence on the accuracy of effective medium theory. Geophys. J. Int. 220 (1), 352–369. https://doi.org/10.1093/gji/ggz452.

Sil, S., 2013. Fracture parameter estimation from well-log data. Geophysics 78 (3), D129–D134. https://doi.org/10.1190/geo2012-0407.1.

Silva, C., de Figueiredo, J.J.S., Chichinina, T., et al., 2019. Experimental characterization of synthetic porous orthorhombic fractured medium: a physical modeling approach. Ultrasonics 94, 82–91. https://doi.org/10.1016/j.ultras.2018.11.015.

Simmons, G., Wang, H., 1971. Single Crystal Elastic Constants and Calculated Aggregate Properties: a Handbook. M.I.T. Press, Cambridge.

Thomsen, L., 1986. Weak elastic anisotropy. Geophysics 51 (10), 1954–1966. https://doi.org/10.1190/1.1442051.

Tosaya, C.A., 1982. Acoustical Properties of Clay-Bearing Rocks. Ph.D. thesis. Stanford University, California.

Wang, Z., 2002. Seismic anisotropy in sedimentary rocks, part 2: Laboratory data. Geophysics 67 (5), 1423–1440. https://doi.org/10.1190/1.1512743.

White, J.E., Martineau-Nicoletis, L., Monash, C., 1983. Measured anisotropy in pierre shale. Geophys. Prospect. 31 (5), 709–725. https://doi.org/10.1111/j.1365-2478.1983.tb01081.x.

Withers, P.J., 1989. The determination of the elastic field of an ellipsoidal inclusion in a transversely isotropic medium, and its relevance to composite materials. Philos. Mag. A 59 (4), 759–781. https://doi.org/10.1080/01418618908209819.

Xu, S., Tang, X., Torres Verdín, C., et al., 2018. Seismic shear wave anisotropy in cracked rocks and an application to hydraulic fracturing. Geophys. Res. Lett. 45 (11), 5390–5397. https://doi.org/10.1029/2018GL077931.

Xu, S., Su, Y., Tang, X., 2020. Elastic properties of transversely isotropic rocks containing aligned cracks and application to anisotropy measurement. Appl. Geophys. 17 (2), 182–191. https://doi.org/10.1007/s11770-020-0820-z.

Yan, F., Vernik, L., Han, D., 2019. Relationships between the anisotropy parameters for transversely isotropic mudrocks. Geophysics 84 (6), R195–R203. https://doi.org/10.1190/geo2019-0088.1.

Zhang, F., Li, X., Qian, K., 2017. Estimation of anisotropy parameters for shale based on an improved rock physics model, part 1: theory. J. Geophys. Eng. 14 (1), 143–158. https://doi.org/10.1088/1742-2140/14/1/143.

Zhao, L., Cao, C., Yao, Q., et al., 2020. Gassmann consistency for different inclusion-based effective medium theories: implications for elastic interactions and poroelasticity. J. Geophys. Res. Solid Earth 125 (3), 1–19. https://doi.org/10.1029/2019JB018328.

Zhao, L., Qin, X., Han, D., et al., 2016a. Rock-physics modeling for the elastic properties of organic shale at different maturity stages. Geophysics 81 (5), D527–D541. https://doi.org/10.1190/geo2015-0713.1.

Zhao, L., Yao, Q., Han, D., et al., 2016b. Characterizing the effect of elastic interactions on the effective elastic properties of porous, cracked rocks. Geophys. Prospect. 64 (1), 157–169. https://doi.org/10.1111/1365-2478.12243.